09

Advanced Optical Metrology

Corrosion

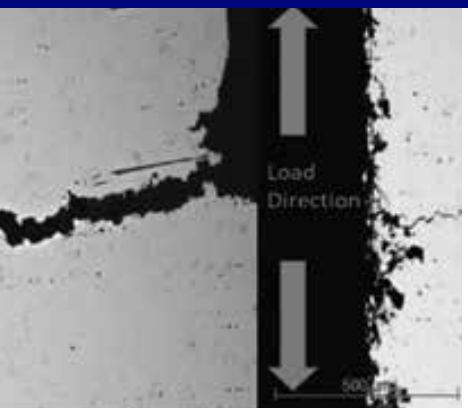

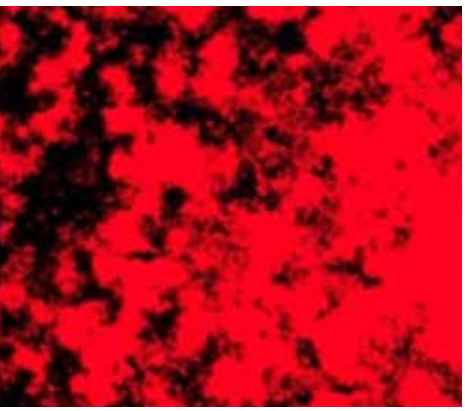

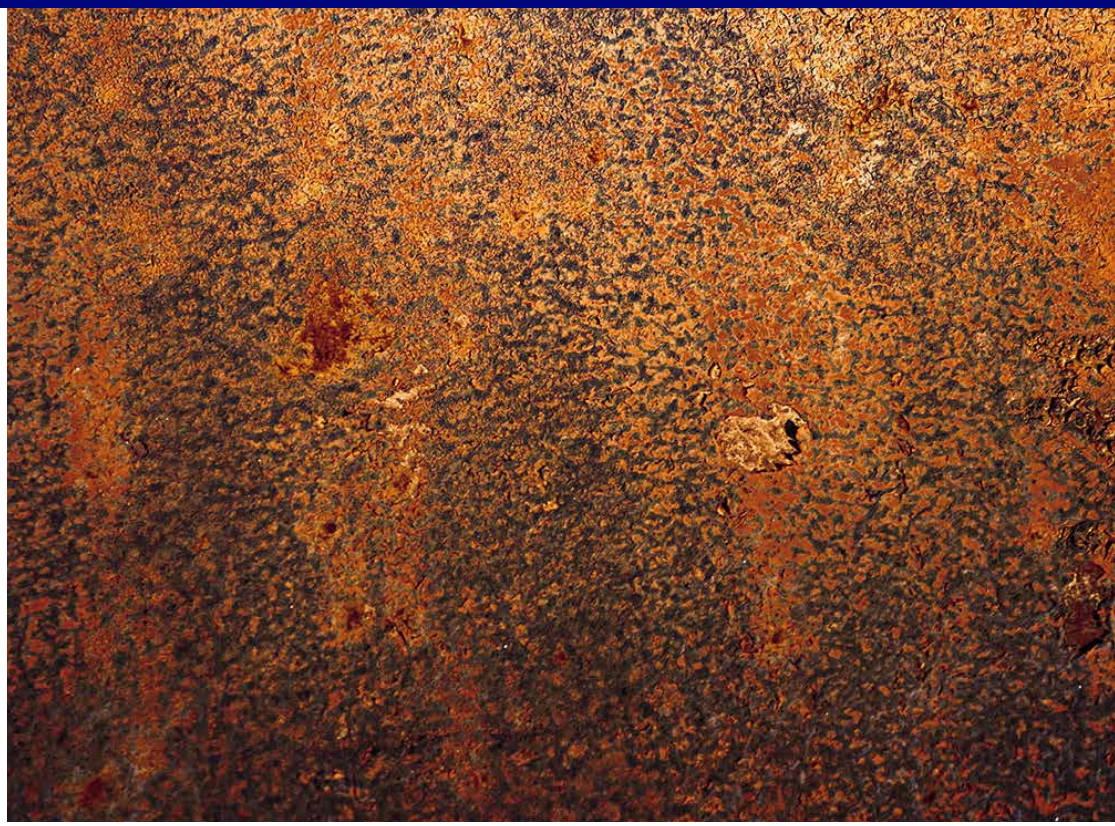

OLYMPUS

WILEY

Contents

Imprint

© Wiley-VCH GmbH
Boschstr. 12,
69469 Weinheim, Germany
Email: info@wiley-vch.de
Editor-in-Chief: Dr. Christina Poggel

Introduction

Corrosion is a natural process consisting of the chemical, biochemical, or electrochemical reaction between a given material and its environment, producing a deterioration of the material and its functional properties. Because of this, corrosion is one of the most common ways that a material fails. Today, the demands on materials' corrosion resistance are increasing to improve operational reliability and extend product life.

Corrosion is an important industrial problem with an estimated global cost equal to approximately 3.4% of the worldwide gross domestic product in 2013.[1] Besides the enormous economic implications, corrosion in structures, critical pieces, and equipment can cause severe accidents, putting people at risk. For example, corrosion fatigue led to the sudden collapse of the Silver Bridge (Point Pleasant, OH) in 1967, which resulted in the loss of 46 lives and cost millions of dollars.[2] Moreover, corrosion can affect health due to pollution from corrosion products, cause the depletion of natural resources, and negatively impact the appearance of materials.

The majority of corrosion processes involve electrochemical redox reaction; however, the corrosion type depends on the environmental conditions and the material's characteristics. One common way to distinguish corrosion is between generalized and localized. The former occurs homogeneously over the entire surface of the material and causes almost total deterioration, making it the most damaging corrosion and, at the same time, the most easy to identify. It is a common problem in the construction industry, affecting ferrous materials that are not alloyed with other stainless materials.

On the other hand, localized corrosion is more difficult to detect, making it a greater risk than **generalized** corrosion. **Localized** corrosion occurs at specific points in a material, depending on its geometry and the environmental conditions. Among the several forms of localized corrosion, *pitting* and *intergranular* corrosion are the most critical. Pitting corrosion[3] occurs mainly in passivated materials. When oxidizing agents accumulate and the pH of the medium increases, the passiva-

tion layer deteriorates, generating corrosion in localized areas. It develops mainly in the direction of maximum deformation and is accompanied by peeling of individual metal particles so that it can be detected visually without the use of instruments. On the other hand, intergranular corrosion[4] is caused by the segregation of impurities at the grain boundaries or by the enrichment/depletion of one or more alloy elements in the areas surrounding the grain boundary. This type of corrosion cannot be detected by the naked eye, so nondestructive control methods must be used.

Another important type of localized corrosion is *stress corrosion cracking*[5] (SCC), which is caused by the synergistic effect of a susceptible material, a corrosive environment, and a minimum stress. SCC results in rapid, catastrophic failure via cracking, which originates in the material surface and propagates as a response to the applied stress.

Corrosion wear (or tribo-corrosion)[6] is the result of a chemical reaction accelerated by temperature. It is usually caused by moisture or other corrosive liquid or gas. In addition, wear can result from the dynamic contact between two surfaces, such as abrasion and erosion. Corrosive wear is defined as the damage caused by the synergistic attack of wear and corrosion when wear occurs in a corrosive environment. Rust, or oxidation, is the best-known form of corrosive wear.

Microbiologically induced corrosion[7] (MIC) is another relevant corrosive route, where an electrochemical process produces the deterioration of a metallic material where microorganisms (bacteria, fungi, or algae) are involved, either initiating, facilitating, or accelerating the corrosive attack mechanism.

Two critical tools to detect and classify corrosion types are optical and electronic microscopes. Samples are treated using standardized processes to reveal the material's microstructure (metals in particular), which are affected by composition, processing conditions, and post-processing variables. The use of microscopy is a key element in failure investigations and usually provides the necessary information to determine the cause of failure. However, the analysis of micrographs is not straightforward. For example, the cracks caused by SCC are very narrow and closed, making visual identification of this type of cracking before a failure difficult. Therefore, the use of instruments that provide high resolution is critical to assess the state of a given material sample.

REFERENCES

[1] *Bowman, E. et al. International Measures of Prevention, Application, and Economics of Corrosion Technologies Study. NACE Int. 1–216 (2016).*

[2] *Davis, J. R. Corrosion: Understanding the Basics. (ASM International, 2000).*

[3] *Vargel, C. Pitting corrosion. in Corrosion of Aluminium 163–183 (Elsevier, 2020). doi:10.1016/B978-0-08-099925-8.00014-4.*

[4] *Vargel, C. Intergranular corrosion. in Corrosion of Aluminium 185–197 (Elsevier, 2020). doi:10.1016/B978-0-08-099925-8.00015-6.*

[5] *Raja, V. S. & Shoji, T. Stress Corrosion Cracking: Theory and Practice. (Elsevier Science, 2011).*

[6] *Li, D. Y. Corrosive Wear. in Encyclopedia of Tribology (eds. Wang, Q. J. & Chung, Y.-W.) 590–596 (Springer US, 2013). doi:10.1007/978-0-387-92897-5_866.*

[7] *Telegdi, J., Shaban, A. & Trif, L. Microbiologically influenced corrosion (MIC). in Trends in Oil and Gas Corrosion Research and Technologies 191–214 (Elsevier, 2017). doi:10.1016/B978-0-08-101105-8.00008-5.*

[8] *Was, G. S. Corrosion and Stress Corrosion Cracking Fundamentals. in Fundamentals of Radiation Materials Science 857–949 (Springer New York, 2017). doi:10.1007/978-1-4939-3438-6_15.*

01 Effect of different amounts of graphene on metal friction and wear during the mixing process

D. Han, K. Wang, H. Bian, *et al.*

ABSTRACT

An internal mixer is one the most common types of rubber-mixing equipment. This device can operate continuously for a long time, and often develops wear on its end face. The end face wear increases the gap between the mixing chamber and the end face, resulting in material leakage, which reduces the mixing effect and impacts the properties of the compound. Therefore, it is important to study the friction and wear of the mixing compound to the metal during the mixing process. In the present study, the influence of the mixing compound with different amounts of graphene (GE) on the friction and wear of the metal end face was analyzed, and the ratio of the corrosion wear to abrasive wear was calculated for the first time.

INTRODUCTION

Rubber has an undeniable role in the economy since it has been widely applied to numerous high-tech and modern technologies. However, raw rubber has low strength, low modulus, poor wear resistance, and fatigue resistance so that it cannot be used in most engineering applications. Accordingly, it is necessary to fill and reinforce the vast majority of rubbers with, for example, carbon black (CB) and silica (SiO_2). However, macromolecular chains form in the packing due to the sticky nature of rubber materials and elastic hysteresis loss inside the rubber packing, thereby producing friction loss and generating considerable heat. Efficiently dissipating the generated heat to the outside leads to internal spirals in the rubber and degrades its performance. Therefore, it is important to improve the thermal conductivity of rubber products to improve their performance and service life under dynamic use. With the diversification of rubber products, many applications need rubber products with antistatic properties, reasonable electrical conductivity, or a gas barrier. Recent investigations have revealed that adding small amounts of nanofillers, such as clay, carbon nanotubes (CNTs), and graphene to the rubber composite can improve the thermal con-

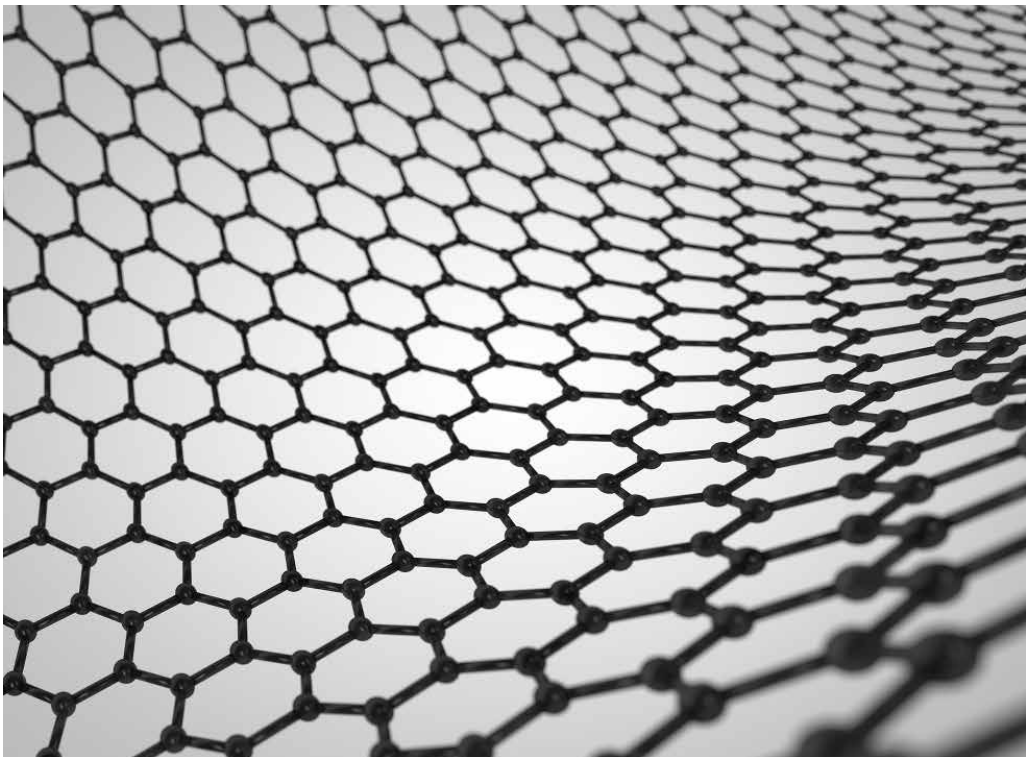

Figure 1: Schematic structure of graphene

ductivity, enhance the heat dissipation capacity, and improve the reinforcement efficiency and functional properties of the final product.

Graphene (GE) is a two-dimensional (2D) crystal with a single atomic layer formed by sp2 hybridization of carbon atoms arranged neatly in cellular lattice structural units. GE is one of the strongest substances known so far, and it is highly ductile and flexible. **Figure 1** shows the schematic structure of GE.

Yong Lin[1] studied the filler–rubber interface interaction in GE/silicon dioxide hybrid styrene–butadiene rubber composites and quantified the number of confinement regions. It was found that the larger the volume fraction of the constraint region, the stronger the interfacial interaction. Moreover, experiments and numerical simulations showed that the higher the volume fraction of the confinement zone, the better the mechanical properties of the composites.

Xumin Zhang[2] studied the thermal conductivity, expansion, and mechanical properties of PrGO/natural rubber (NR) nanocomposites. It was found that as the amount of PrGO in the composite increases, the thermal conductivity and energy storage modulus of PrGO/NR nanocomposite increases, while solvent absorption decreases. Moreover, adding 3 phr of PrGO increases the tensile strength and tear strength of nano-NR composites by 23% and 150%, respectively.

Hong Zhu[3] studied the effect of GE/silicon dioxide nanocomposites on the properties of SSBR/BR. It was found that adding reduced graphene oxide (rGO) improves the mechanical properties of SSBR/BR.

Yanping Wu[4] studied the mechanical and tribological properties of GE-reinforced rubber composites. The results showed that the mechanical properties of SSBR–BR composite filled with FGS were substantially better than those of the unfilled and equivalent filler-loaded graphene oxide (GO) and rGO-filled SSBR–BR composites. Moreover, it was found that the addition of GO, rGO, and FGS decreases the wear resistance of SSBR-BR composites.

GE/rubber composites have become a hot topic in the rubber field in recent years.[5–11] In this article, the effect of adding different amounts of GE on the friction and wear of the end face metal during the mixing process was studied.

EXPERIMENTS

Instruments

Hake internal mixer, BL-6157 Double Roll Mill, ZT-2588S steam generator, RPA 2000 Rubber Processing Performance Analyzer, DisperGRADER Dispersion Meter, LEXT™ OLS5000 3D laser measuring microscope (Olympus® Japan), CSM-Friction and Wear Tester.

Formula

The formula is shown in **Table 1**.

Mixing process

In order to ensure the accuracy of the experiment, the test sample was made by pressing through a double-roller mill. To ensure the smoothness of rubber samples, samples pressurized by the double roller mill were put into the grinding tool to obtain a smooth surface and reduce the influence of surface roughness on the friction coefficient.

Test methods

1. The Panye effect[12-13] refers to the phenomenon that the dynamic modulus of filled rubber decreases sharply with the increase of strain. This phenomenon is usually used to reflect the dispersion of packing. The deformation of six rubber compounds was scanned by a rubber analyzer, and the distribution of dynamic modulus G0 changing against strain was obtained.

2. The Silanization reaction index is an important to measure the degree of silane modification of silica. A rubber processing analyzer was used to test the silylation reaction index. The greater the silanization reaction index, the higher the degree of silanization reaction, and the better the overall properties of the rubber compound.

3. Friction and wear testing was carried out using a CSM. To this end, the experimental pressure, rotational speed, and the test time were set to 5 N, 70 rpm, and 120 min, respectively. In order to study the wear condition of the internal mixer end face, the same metal grinding head material and end face material were used in the experiment. To ensure complete silanization, the mixing temperature was kept at 145–155 °C (293–311 °F) for 1 min. The temperature of CSM was set to 150 °C (302 °F) to ensure the reliability of the experiment. CSM is shown in **Figure 3**.

4. 3D morphology observation: The metal surface morphology was observed by using a 3D laser measuring microscope (OLS5000, LEXT, Olympus), where the wear amount was obtained by measuring the volume reduction of the metal grinding head.

5. Dispersion test: A carbon black dispersion tester was used to test the degree of disper-

Substance	C1	C2	C3	C4	C5	C6
NR	100	100	100	100	100	100
Nanosilicon dioxide	30	30	30	30	30	30
GE	0	0	1	2	3	4
ZnO	2	2	2	2	2	2
Anti-aging agent 4020	2	2	2	2	2	2
SAD	2	2	2	2	2	2
TESPT	0	5	5	5	5	5
DPG	1.3	1.3	1.3	1.3	1.3	1.3
S	1.3	1.3	1.3	1.3	1.3	1.3
CZ	1.8	1.8	1.8	1.8	1.8	1.8

Table 1: Chemical composition of GE/natural rubber composites

Figure 2: Configuration of the CSM wear test device

sion and obtain the dispersion value based on the ASTM D7723 standard (**Figure 2**).

SILANIZATION REACTION MECHANISM

Bis(3-triethoxysilylpropyl)tetrasulfide (TESPT) is a bifunctional silane coupling agent. Arkles[14] proposed a four-step reaction model based on the coupling process of TESPT:

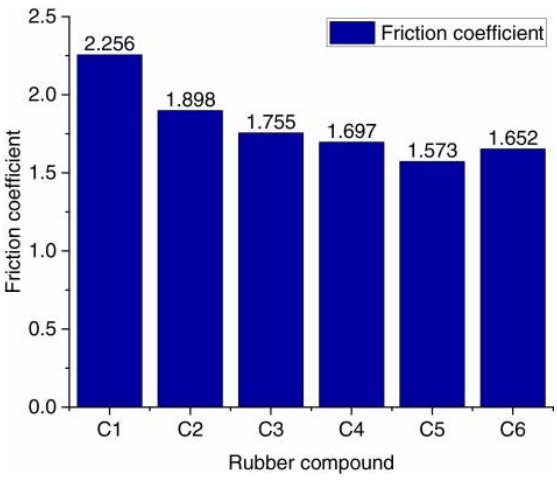

Figure 3: Average friction coefficient in different compounds

1. Three Si-OR groups connected with silicon are hydrolyzed to Si OH;

2. Si-OH is dehydrated and condensed into oligosiloxane containing Si OH;

3. Si-OH in the oligomer forms a hydrogen bond with OH on the substrate surface;

4. A covalent bond is formed with the substrate along the dehydration reaction in the heating curing process, but only one of the silicon hydroxyl groups of silane is bonded with the substrate surface at the interface, leaving two Si-OHs and condensation with Si-OHs in other silanes or free states. Therefore, the two materials with different properties can be coupled interfacially by using a silane-coupling agent, improving the composite properties, increasing the bonding strength, and obtaining a new composite with excellent performance and reliability.

Most wear occurs in the final mixing process, where the temperature is high and the mixer is in a closed state. In this high-temperature environment, ethanol vapor could not overflow the mixer, thereby resulting in corrosion wear. Accordingly, high-temperature, vapor-induced corrosion should be considered in investigating the friction and wear of the end face of the mixer. However, it is an enormous challenge to disassemble the end face of the internal mixer during the actual process and measure the quality of ethanol vapor. During the experiment on the CSM friction and wear testing machine, high-temperature ethanol vapor is sprayed on the surface of the mixing glue and metal in proportion to the degree of silylation reaction to simulate the mixing situation of the internal mixer.

RESULTS

Dispersion analysis of the packing

Payne effect

The rubber compounds without GE and TESPT could not have a silanization reaction. Consequently, a chemical connection does not form between the silica and rubber, resulting in a poor silica dispersion. With the increase of the amount of GE, the Payne effect of the rubber compound increases gradually. The GE could intercalate between silica particles, isolate silica particles, and prevent silica agglomeration. Moreover, GE-intercalated silica affects the silica dispersion. Additionally, as the GE continuously increases,

the agglomeration of GE became intensified, thereby increasing the Payne effect.

Dispersion comparison

The worst silica dispersion in the rubber compound belongs to the case without TESPT, which also has the highest silica aggregates. It is observed that as the amount of GE in the compound increases, the aggregate of GE increases, while the dispersion of the rubber compound decreases. The GE has a 2D crystal with a single atomic layer, which is composed of carbon atoms connected by sp2 hybridization. Therefore, GE intercalates silica particles, and its planar structure can hinder the silanization reaction.

Silanization reaction index

For the rubber compound of the silica formula system, the greater the silanization reaction index, the higher the degree of the silanization reaction, the more the overall dispersion of silica and rubber molecules and the better the silica dispersion. For the same formula system, the proportion of silanization reaction index reflects the proportion of silanization reaction product ethanol. In this regard, RPA 2000 was used, and the silanization reaction indices of five rubber compounds are evaluated.

The silylation reaction index of the mixers decreases gradually with the increase of the amount of GE. The products of the silanization reaction are ethanol and water. The wear of metal caused by water vapor has been studied, so the effect of produced ethanol from the silanization reaction was studied in this experiment. In the actual production process, it is a challenge to disassemble the internal mixer and measure the wear of the internal mixer face in real time, and it is not feasible to measure the quality of the produced ethanol vapor in the mixing process. In this experiment, when the wear test was carried out on the CSM, high-temperature ethanol vapor was sprayed on the surface of the rubber compound in proportion to the degree of the silylation reaction to simulate the real mixing process.

Effect of adding different amounts of GE on metal friction and wear

The coefficient of friction

Figure 3 reveals that the largest friction coefficient can be achieved in the rubber compound without TESPT and GE. This is because the silanization reaction of silica could not occur without adding TESPT in the mixing process. Accordingly, silica aggregates do not form easily among silica molecules. After adding TESPT, a silanization reaction occurs in the mixing process and a chemical bond establishes between silica and rubber. Accordingly, the silica dispersion increases and the aggregate of silica decreases. As a result, the friction coefficient of the C2 compound is significantly reduced compared to that of the C1 compound.

Three-dimensional morphology of metals

Comparing A1 and B1 in **Figure 4**, a large number of scratches appear on the metal surface after friction. Moreover, comparing A2 and B2, more pits appear on the height contour of the metal surface after friction, and the original height contour peaks mostly flatten. A large amount of silica aggregates in the rubber compound. Since silica has high hardness, the metal surface is worn so that many scratches appear on the metal surface after friction.

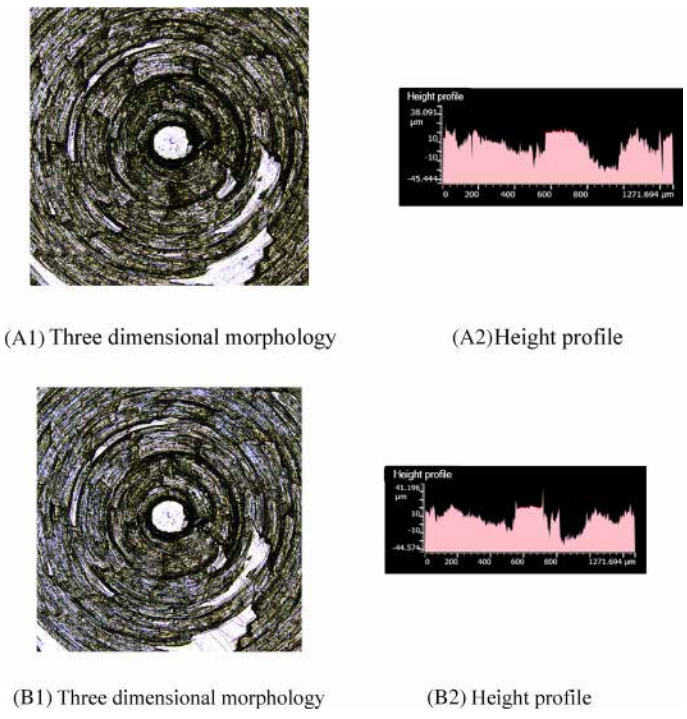

Figure 4: The surface morphology of the metal before and after the friction of the rubber compound without GE and TESPT (A1 and A2 are before friction; B1 and B2 are after friction). GE, graphene; TESPT, bis(3-triethoxysilylpropyl) tetrasulfide.

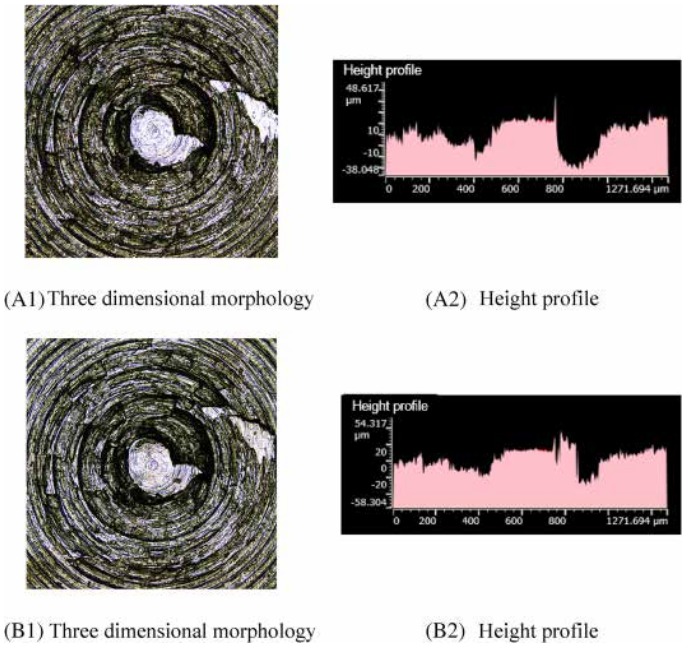

Figure 5: The surface morphology of the metal before and after the friction of the rubber compound without GE (A1 and A2 are before friction; B1 and B2 are after friction).

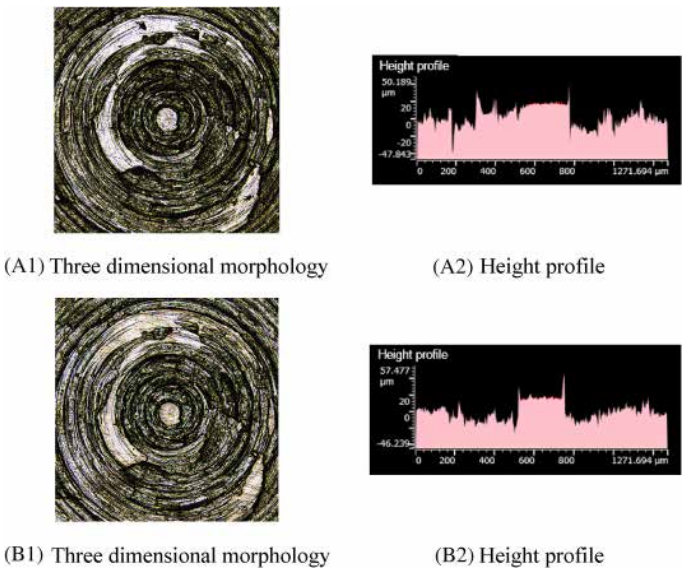

Figure 6: Surface morphology of the metal before and after friction with 1 phr of GE.

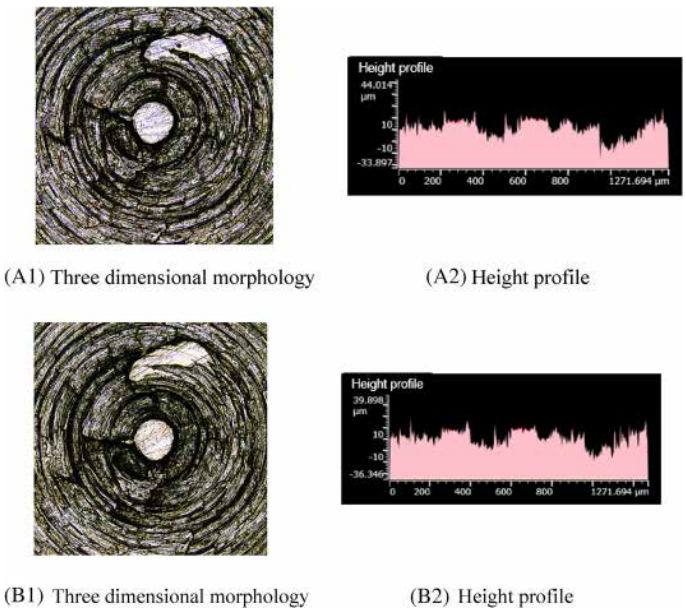

Figure 7: Surface morphology of the metal before and after friction with 2 phr of GE (A1 and A2 are before friction; B1 and B2 are after friction).

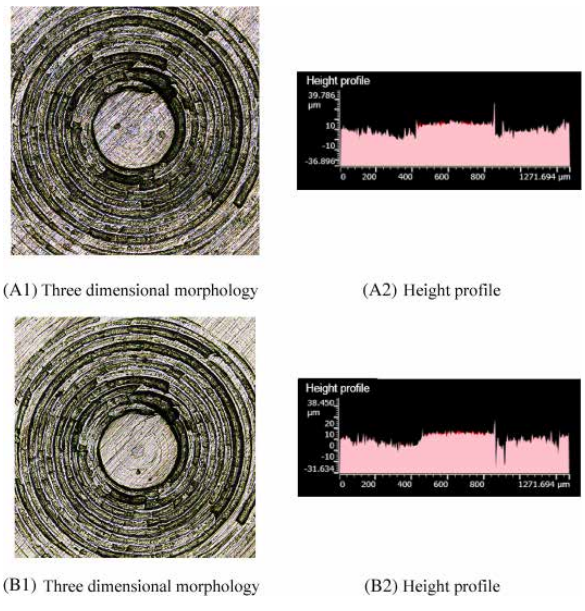

Figure 8: The surface morphology of the metal before and after friction of the rubber compound with 3 phr of GE (A1 and A2 are before friction; B1 and B2 are after friction).

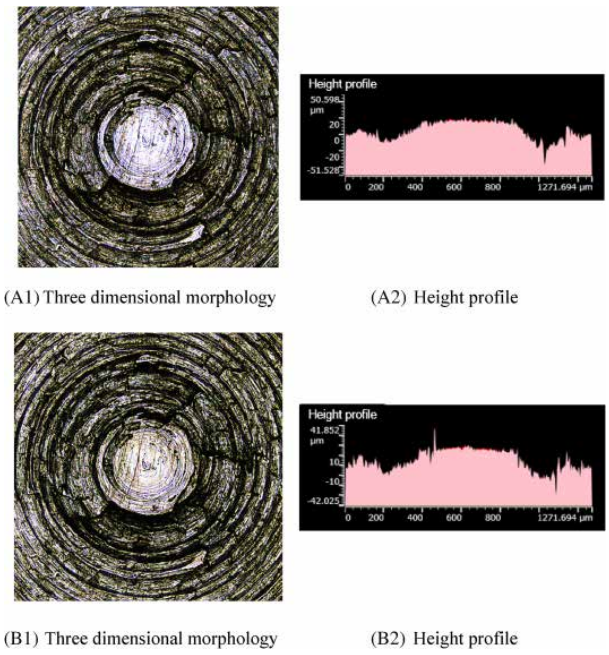

Figure 9: The surface morphology of the metal before and after friction of the rubber compound with 4 phr of GE (A1 and A2 are before friction; B1 and B2 are after friction).

Comparing A1 and B1 in **Figure 5**, there are fewer scratches on the metal surface after friction. Furthermore, **Figure 5** A2, B2 indicates that the height profile of the metal surface partially flattens after friction so that the peak of the height profile changed greatly. When TESPT is added to the compound mixture, the number of silica aggregates is lower. As a result, scratches on the metal surface reduce. However, with the progress of the silanization reaction, the temperature of ethanol vapor gradually increases and has a corrosive effect on metal. Considering the friction of the mixing adhesive on metal, this phenomenon results in the production of highly corrosive wear. Therefore, although there were few scratches on the metal surface, the height profile of the metal surface changed greatly, and the wear vapor-induced corrosion becomes the worst case.

Comparing A1 and B1 in **Figure 6**, more scratches appear on the metal surface after friction. Furthermore, **Figure 6** A2, B2 indicates that a large part of the height contour peaks of the metal surface flatten and pits appear in the height contour. GE intercalates silica particles, and its planar structure hinders the silylation reaction. Therefore, with the addition of 1 phr GE, the silanization reaction index and the amount of high-temperature ethanol vapor decrease, and the amount of corrosive wear decreases. Since GE has reasonable toughness and the intercalation of GE between silica particles hinders the contact between silica aggregates and metals, the amount of abrasive wear reduces.

Figure 7 A1, B1 shows that there are fewer scratches on the metal surface after friction. **Figure 7** A2, B2 illustrates that a small number of height peaks on the metal surface flatten after friction, and the overall change of height contour peaks is negligible. This phenomenon mainly originates from GE intercalation between silica particles, which further hinders the contact between silica aggregates and the base metal. It is observed that as the GE content increases, the corrosion wear decreases significantly.

Similar to previous parts, **Figure 8** A1, B1 shows that there are fewer scratches on the metal surface after friction. Moreover, **Figure 8** A2, B2 indicates that the height profile of the metal surface slightly changes after friction. This phenomenon may be attributed to the GE lamellae further hindering the contact between silica aggregates and metals. In this case, the metal contacts with the silica aggregate only when a piece of GE was worn completely, and then another GE layer appears. As the GE content increases, the silylation reaction index further decreases and the high-temperature steam decreases, thereby reducing the corrosion wear.

Figure 9 A1, B1 shows that there are more scratches on the metal surface after friction. **Figure 9** A2, B2 shows that after friction, part of the height contour peak of the metal surface flattens, pits appear in the height contour, and the overall height contour changes greatly. When 4 phr GE is added to the compound, a large amount of agglomeration between GE and TESPT is wrapped by GE, which hinders the silanization reaction, thereby producing a small amount of high-temperature ethanol vapor and a low amount of corrosive wear. Meanwhile, the hindrance of silica particles by GE sheets reduces, and a large number of silica aggregates appear. Consequently, the rubber compound with 4 phr GE has the largest abrasive wear on the metal.

Metal wear volume
TESPT has the largest wear on the metal. It is observed that with the gradual increase of the GE content, the wear of the rubber compound on the metal decreases first and then increases. The minimum wear can be achieved when 3 phr GE was added. When the amount of GE exceeds 3 phr, the wear amount of the rubber compound on the metal increases.

TESPT was an important raw material for silanization reaction. There is no TESPT in compound C1, so a silanization reaction cannot occur. Therefore, silica dispersion in this compound is very poor so that more and large silica aggregates appear. The friction of silica aggregates on the metal is the most important source of abrasive wear. Accordingly, the rubber compound C1 has great abrasive wear on the metal. After adding TESPT, the silica dispersion increases so that the silica aggregate decreases. More specifically, the metal wear of C2 rubber compound reduces by 7.22% compared with that of the C1 rubber compound.

As the amount of GE further increases, the GE lamellae further hinder the contact between silica aggregates and metals, and the wear of the rubber compound on the metal decreases. However, when the amount of GE exceeded 3 phr, a large number of GE agglomerates and GE encapsulated TESPT, which hindered the silanization reaction. Accordingly, small amounts of high-temperature steam and corrosive wear are produced. With a large number of GE aggregates, the blocking effect of GE sheets on silica particles is reduced, and a large number of silica aggregates appear in the rubber compound. Among the studied compounds, the rubber compound with 4 phr GE has the largest wear capacity on the metal.

Proportion of corrosive and abrasive wear
The CSM friction and wear tests were carried out on the rubber compound without spraying high-temperature ethanol vapor, so there is no corrosive wear so that abrasive wear is the only wear mechanism.

It was found that GE intercalates silica particles, hinders the movement of silica particles, and reduces the silica dispersion. Moreover, GE laminate could wrap TESPT and reduce the occurrence of silylation reaction. Therefore, as the GE content increases, the degree of the silanization reaction decreases. Meanwhile, the production of high-temperature steam decreases, thereby reducing the proportion of corrosion wear to abrasive wear.

Roughness changes before and after friction
The largest surface roughness can be achieved for the compound with no TESPT. This may be attributed to the absence of silanization reaction so that the silica aggregates. On the other hand, with the increase of the amount of GE, the silanization reaction decreases so that silica aggregates. Therefore, with the increase of the amount of GE, the surface roughness gradually increases after the metal friction was rubbed by the rubber compound.

CONCLUSION

Based on the results, it was found that as the amount of GE in the rubber compound increases, the proportion of abrasive wear on the metal increases, the proportion of corrosive wear on the metal decreases, and the metal wear decreases first and then increases. With the increase of the GE content, the production of high-temperature steam and the proportion of corrosive wear decreases.

The lowest metal wear can be achieved when the GE amount is 3 phr. However, when the GE amount exceeds 3 phr, a large number of GE agglomerates and GE encapsulated TESPT, which hinders the silanization reaction, resulting in a small amount of high-temperature steam production and a low amount of corrosion wear. However, with a large number of GE aggregated, the blocking effect of GE sheets on silica particles reduces, and a large number of silica aggregates appear in the rubber compound. Therefore, the mixing compound with 4 phr GE has greater wear on the metal.

ACKNOWLEDGMENTS

This research was funded by Key Technology and Equipment for Intelligent Green Manufacturing of Rubber Products, grant number ZR2016XJ003; Natural Science Foundation of Shandong Province, grant number ZR2019BEE056; Polymer Material Intelligent Manufacturing Innovation Team, grant number 2019KJB007; Key R & D Plan of Shandong Province, grant number 2019GGX102018; Shandong Provincial Natural Science Foundation, grant number ZR2020QE207;and also funded by Hunan Province 121 innovative talents project. The funders contributed to the work. The authors would like to thank the Shandong Provincial Key Laboratory of Polymer Material Advanced Manufacturing Technology for their support in this experiment.

REFERENCES

[1] *Y. Lin, S. Liu, J. Peng, L. Liu, Appl. Sci. Manuf. 2016, 86, 19.*

[2] *X. Zhang, J. Wang, H. Jia, S. You, X. Xiong, L. Ding, Z. Xu, Compos. Part B 2016, 84, 121.*

[3] *H. Zhu, Z. Wang, X. Huang, F. Wang, L. Kong, B. Guo, T. Ding, Compos. Part B 2019, 175, 107027.*

[4] *Y. Wu, L. Chen, S. Qin, J. Li, H. Zhou, J. Chen, J. Appl. Polym. Sci. 2017, 134, 44970.*

[5] *D. S. Han, S. Zhang, K. Wang, Y. Pan, D. Zhu, J. Appl. Polym. Sci. 2021, 138, e50761.*

[6] *S. Geng, P. Wang, T. Ding, Compos. Sci. Technol. 2011, 72, 36.*

[7] *M. A. Tarawneh, S. H. Ahmad, S. Y. Yahya, R. Rasid, S. Y.,Noum, J. Reinf. Plast. Compos. 2011, 30, 363.*

[8] *P. M. Ajayan, O. Stephan, C. Colliex, D. Trauth, Science 1994, 256, 1212.*

[9] *L. Shen, X. Zhang, Y. Lei, M. Liang, Y. Chen, W. Chen, H. Zou, Polym. Compos. 2021, 1. https://doi.org/10.1002/pc.26165.*

[10] *H. Yan, T. Yuanzheng, J. Theor. Comput. Chem. 2013, 12, 1.*

[11] *X. Li, Y. Xia, Acta Mater. Compos. Sin. 2015, 32, 1007.*

[12] *Z. Xu, Y. Song, Q. Zheng, Polymer 2019, 185, 121953.*

[13] *J. Flambard, F. Carrette, C. Monchy-Leroy, E. Andrieu, L. Laffont, J. Nucl. Mater. 2021, 543, 152562.*

[14] *B. Arkles, J. R. Steinmetz, J. Zazyczny, P. Mehta, J. Adhes. Sci. Technol. 1992, 6, 193.*

02 The effect of cathodic polarization on the corrosion behavior of X65 steel in seawater containing sulfate-reducing bacteria

M. Lv, X. Li, M. Du

ABSTRACT

Sulfate-reducing bacteria (SRB) are one of the main reasons for the accelerated corrosion of steel. Cathodic polarization is an effective and economic method against marine corrosion, including microbiologically induced corrosion. However, the interaction between cathodic polarization and microbial activity has not been well defined. In this study, a fluorine-doped tin oxide electrode is used to study the effect of cathodic current on SRB cells. The results clearly show that the attachment degree of SRB is dependent on the electric quantity and current intensity. The large electric quantity and high cathodic current can effectively inhibit bacterial attachment and subsequent biofilm formation. Furthermore, the effect of cathodic potential on the corrosion behavior of X65 steel in the presence of SRB is systematically investigated. Results show that the impressed charges, the increase of pH, and the formation of calcareous deposits on the electrode surface at the cathodic potential of –1,050 mV/SCE inhibit the attachment of SRB. In turn, the presence of SRB also interferes with the electrochemical reactions that occur during the polarization process, thus increasing the cathodic current. The interaction between SRB-induced corrosion and the process of preventing corrosion by various cathodic potentials is discussed.

INTRODUCTION

Cathodic polarization is an effective and common method to prevent corrosion of metallic structures and marine facilities.[1] The protection potential of –770 mV/SCE at room temperature can resist the naturally occurring corrosion current and prevent the steel from corrosion risk.[2]

However, there have been some unaccountably external corrosion problems, and in many cases, the presence of microorganisms (e.g., sulfatereducing bacteria [SRB]) is associated with these problems.[3] Microbiologically induced corrosion (MIC) is a bioelectrochemical process that initiates or accelerates the corrosion reaction by microbial activity.[4,5] MIC induced by SRB has been extensively investigated in the literature. Zhu *et al.*[8] found that the corrosion rate of X56 steel in the sea mud containing SRB was 10-fold higher than in the sea mud without SRB. SRB can reduce sulfate (SO_4^{2-}) to sulfide (H_2S, HS^-), which may indirectly contribute to the accumulation of corrosive sulfide and organic acid end products, causing localized pitting of metals.[9] Several mechanisms have been proposed to explain the role of SRB in MIC,[10-15] including cathodic depolarization, local corrosive cell, and metabolite-induced corrosion. Cathodic depolarization accelerates the cathodic reaction due to the consumption of cathode hydrogen via hydrogenase biocatalysis by SRB, which increases the electron demand of the anode and associated corrosion.[16,17] Metal sulfides produced by SRB metabolism are electrically conductive and cathodic with respect to steel, forming aggressive corrosion cells.[14] Recently, it has been suggested that SRB can acquire the energy needed by obtaining electrons via direct or indirect contact with the steel substrate, leading to more severe corrosion.[18]

Studies have shown that the electrochemical changes at the metal–solution interface during cathodic polarization influence the composition and concentration of chemical species and the attachment of microorganisms. [19-21]. Sun *et al.*[22] studied the effects of SRB on cathodic polarization of Q235 steel in the soils and showed that the number of SRB in soils decreased, and the protection efficiency increased with the shift of applied potential to a negative direction. Saravia *et al.*[23] stated that there was a decrease in the number of attached cells when the cathodic potential was applied in the initial stages of biofilm formation. Olivares *et al.*[24] , however, presented opposite findings. They found that the SRB population on polarization potential-applied pipeline steel (–850mV vs. Cu/CuSO4) was twice that of without cathodic polarization. Liu *et al.*[25] confirmed that the application of cathodic polarization did not affect the growth of planktonic bacteria, but it was beneficial to the adhesion of SRB cells to steel in the extracted soil solution.

To date, the interaction between cathodic polarization and microbial activity has not been well clarified due to the complicated processes occurring at the cathodically polarized surface. The objective of this study was to investigate the effect of cathodic polarization on microbial attachment and the effect of various cathodic potentials on the corrosion of X65 steel in sea water containing SRB.

MATERIALS AND METHODS

Materials

Fluorine-doped tin oxide (FTO) conducting glass (10 × 20 mm) was used for fluorescent confocal imaging to study the effect of cathodic current on SRB cells. Another specimen was X65 pipeline steel, which was used to study the effect of cathodic potential on corrosion in the presence of SRB. The X65 specimen (10 × 10 × 3 mm) was machined and embedded in epoxy resin, leaving a work area of 1 cm^2 for electrochemical measurement. The work face of the specimen was mechanically abraded with silicon carbide metallurgical papers sequentially, degreased by anhydrous ethanol, and then dried in high-purity nitrogen. All the prepared specimens were sanitized for 30 min using an ultraviolet lamp before use to ensure that there was no contamination by other bacteria.

SRB strain and its inoculation process

In this study, SRB (i.e., *Desulfovibrio caledoniensis*) were isolated from the rust layers of carbon steel immersed in seawater (Qingdao, China) and identified by polymerase chain reaction (PCR) amplification of 16S ribosomal DNA. SRB strains were cultivated in a constant-temperature incubator at 30 °C (86 °F) for 5 days. Then, 5 ml of SRB strains were transferred into 500 ml seawater (containing the whole culture medium) to prepare the test solution. Before inoculation, the medium was deoxygenated with high-purity nitrogen for 30 min and then sterilized by autoclaving at 121 °C (249.8 °F) for 20 min. The living cell num-

ber of SRB was calculated by the most probable number ASTM standard D4412-84.

Surface analysis

Bacterial attachment on the FTO glass electrode surface in situ was characterized using a confocal laser scanning microscope (FLUOVIEW™ FV1000; Olympus®). Before observation, the electrodes were soaked in sterile phosphate-buffered saline solution containing 5% (v/v) glutaraldehyde for 30 min and then stained with a fluorescent dye (DAPI) for 30 min in darkness.

The surface morphologies of X65 steel were observed using a scanning electron microscope (SEM; JSM-6700F; JEOL). The elemental composition and valence of the corrosion products were measured by energy-dispersive X-ray spectroscopy (EDS; JSM-6700F; JEOL) and X-ray photoelectron spectroscopy (XPS; ESCALAB 250Xi; Thermo Fisher Scientific).

A three-dimensional measuring laser microscope (LEXT™ OLS4000; Olympus, Tokyo, Japan) was used to characterize the surface morphology of the corroded steel specimens after the removal of corrosion products. Before the corroded surface examination, the specimens were taken from the test solution and subsequently immersed in a pickling solution containing corrosion inhibitor (hexamethylenetetramine) for 5 min, then rinsed with distilled water, cleaned with absolute ethanol, and finally dried with a nitrogen gas stream.

Electrochemical measurements

All the electrochemical measurements were performed using a Gamry electrochemical workstation. A saturated calomel electrode and a platinum plate were used as the reference and counter electrode, respectively. X65 steel was cathodically polarized for 14 days at the potentials of –800 and –1,050 mV/SCE, respectively. In addition, the cathodic potentials of –1,050 mV/SCE (the first 7 days) to –800 mV/SCE (the last 7 days) and –800 mV/SCE (the first 7 days) to –1,050 mV/SCE (the last 7 days) were also applied. Electrochemical impedance spectroscopy (EIS) was performed when the open circuit potential (OCP) reached a steady state. The applied polarization potential was switched off for a certain period to allow the potential to return to OCP, and then the EIS measurement was performed. After the EIS test was completed, the applied polarization potential was again switched on. EIS was obtained in the frequency range of 105–10–2 Hz, and the amplitude of the sinusoidal voltage signal was 10 mV. The EIS data were analyzed using Zview2 software with a suitable equivalent circuit model. All electrochemical experiments were carried out at 25 °C (77 °F) in an airtight system and repeated at least three times to check the reproducibility.

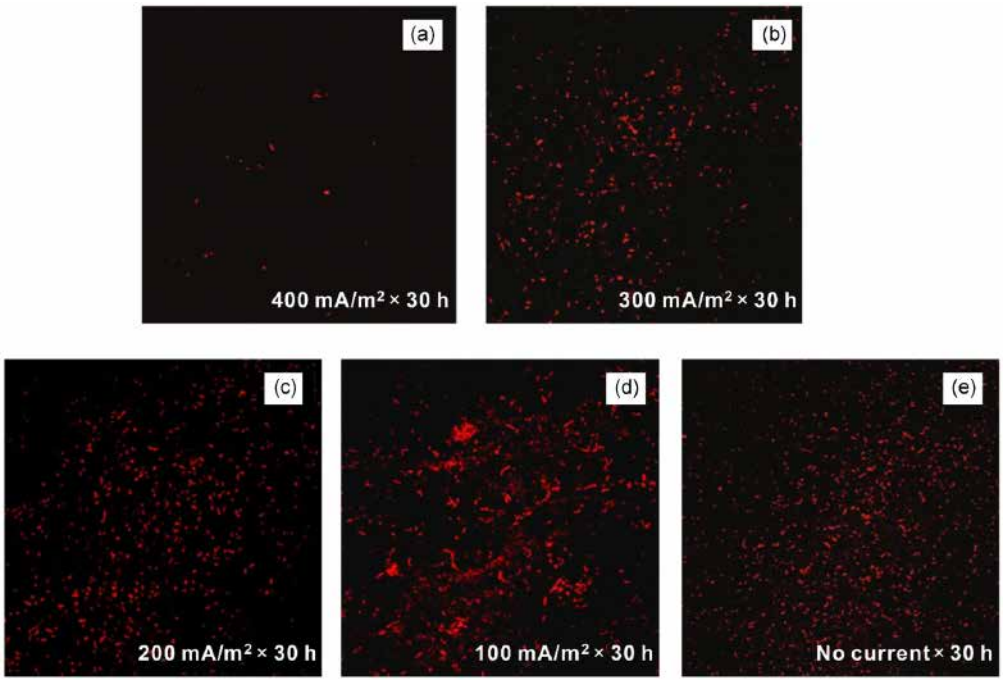

Figure 1: Fluorescent images of sulfate-reducing bacteria cells attached to the surface of the fluorine-doped tin oxide electrode after applying different cathodic current for 30 hr: (a) 400 mA/m^2, (b) 300 mA/m^2, (c) 200 mA/m^2, (d) 100 mA/m^2, (e) no current.

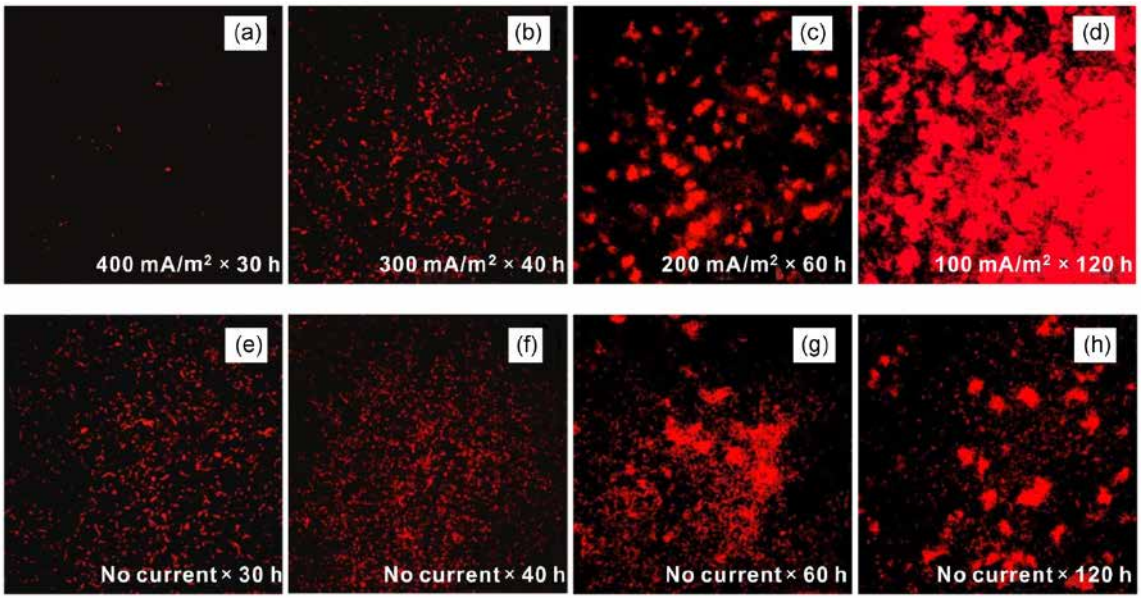

Figure 2: Fluorescent images of sulfate-reducing bacteria cells attached to the surface of the fluorine-doped tin oxide electrode after applying the same quantity of electric charge: (a) 400 mA/m²× 30 hr, (b) 300 mA/m²× 40 hr, (c) 200 mA/m² × 60 hr, (d) 100 mA/m² × 120 hr, and the control system: (e) No current × 30 hr, (f) No current × 40 hr, (g) No current × 60 hr, and (h) No current × 120 hr.

RESULTS AND DISCUSSION

The growth curve of SRB

The growth curve of SRB displayed a typical three-stage growth cycle. The first stage, which lasted for 1–4 days, is the exponential growth phase. During this stage, the number of active SRB increased rapidly. The growth stage from 5–10 days is the stationary phase. During this stage, the number of SRB increased and decreased equally, so the total number of SRB was large and stable. After 10 days, the growth process reached the death phase, during which the number of SRB decreased dramatically due to the lack of essential nutriments.

The effect of cathodic current on bacterial attachment

After applying different cathodic current for 30 hr, the effect of electric quantity on the attachment of SRB to the FTO electrode was studied, as given in **Figure 1**. The results showed that when more negative charges were applied, less SRB cells were attached. When the electric quantity of 400 mA/m² ×30 hr) was applied, the attachment of SRB on the electrode surface was significantly less than that of the control system (no current). The electric quantities of 300 mA/m²×30 hr and 200 mA/m²×30 hr had a little influence on the adhesion degree of SRB. Wilson *et al.*[26] have reported that cell surface was negatively charged by ionized phosphoryl and carboxylate substituents under normal conditions. Therefore, SRB cells may be repelled by a large build-up of negative charges on the surface of cathodically polarized electrode.[27] When the electric quantity applied to the FTO increased, there was an increase in the electrostatic repulsion. Consequently, the attachment of SRB was inhibited by the large electric quantity (400 mA/m²×30 hr). Interestingly, when a relatively small electric quantity was applied to the surface of the FTO electrode (**Figure 1d**), the number of attached SRB was more than that of the control system.

These results indicated that electric quantity was an important factor affecting the attachment of SRB. However, when the same electric quantity was applied, was microbial attachment related to current intensity? **Figure 2** shows the attachment of SRB on the surface of FTO electrode at the same electric quantity, but at various current densities. As shown in **Figure 2a–d**, the number of attached SRB cells markedly decreased with the increase of current density. The high cathodic current of 400 mA/m² effectively inhibited bacterial attachment and subsequent biofilm formation. It was further demonstrated that although the same quantity of electric charge was applied, a low current of 100 mA/m² pro-

moted bacterial attachment. When the electrostatic force between FTO and SRB was insufficient, cathodic polarization promoted the evolution of hydrogen, which contributed to the growth of hydrogenase-positive SRB.[28] Thus, there was an increase in SRB cells attached to the FTO at 100 mA/m^2. Given the above analysis, the attachment of SRB can be properly controlled by adjusting the electric quantity in combination with a high current.

The effect of cathodic potential on the corrosion of X65 steel in SRB-containing seawater

Most microorganisms tend to colonize, proliferate, and form a biofilm on metal surfaces, resulting in MIC. The initial attachment of bacteria is a crucial step, which lays the foundation for the formation of biofilm. Therefore, it is important to prevent or delay bacterial attachment and growth for corrosion control. In marine engineering, the commonly used criterion for the effectiveness of cathodic protection is the polarization potential. Therefore, –800 and –1,050 mV/SCE were selected as the applied potentials for this study. In addition, the cathodic potential ranging from –1,050 to –800 mV/SCE was impressed to X65 steel, that is, the negative potential of –1,050 mV/SCE was used to inhibit bacterial attachment in the rapid growth phase of SRB, and the inhibition effect of –800 mV/SCE on corrosion in the later stage was studied. The cathodic potential shifted negatively from –800 to –1,050 mV/SCE.

OCP monitoring

The different OCP variations in both systems, SRB-inoculated medium and sterile medium, indicated that the activity of SRB affected the corrosion process of X65 steel. The OCP of X65 steel in the sterile system remained stable at around –670 mV/SCE. In contrast, the OCP values in the SRB system fluctuated significantly and moved negatively to –718 mV/SCE after 5 days. It was possible that the activity of SRB changed the electrochemical process, providing a high driving force for the corrosion of X65 steel. Subsequently, the OCP moved to a positive direction and stabilized at the potential of around –640 mV/SCE.

EIS measurements

For specimens in the SRB-containing medium at OCP, the diameter of the Nyquist plot increased from 1 to 4 days, then decreased with time gradually, and afterward increased again after 14 days. The increase of the Nyquist plot diameter was attributed to the formed biofilm and corrosion products providing some protection to the steel in the initial incubation time, which hindered the charge transfer process. The decrease of the Nyquist plot diameter indicated that the high SRB activity accelerated the corrosion of X65 steel. Meanwhile, the production of corrosive agents such as sulfide, organic acids, and/or inorganic acids by SRB promoted the anode dissolution of metal.[7,15] After 14 days, the Nyquist plot diameter increased again due to the decline in the SRB activity. The peak of the phase angle shifted to a high frequency before 4 days and then to a low frequency. This situation indicated the formation of a protective corrosion product film, followed by the breakdown of the film. In the presence of SRB at cathodic potential of –800 mV/SCE, the diameter of the Nyquist plot was several times smaller than that at OCP, indicating that this cathodic potential had no protective effect on SRB-induced corrosion. When the potential of –1,050 mV/SCE was applied on the electrode, the diameter of Nyquist plot increased gradually. The impedance values were larger than that at OCP, which indicated that this potential effectively slowed down the corrosion in the presence of SRB. The potential ranging from –1,050 to –800 mV/SCE also offered some protection to the specimen toward further corrosion. The Nyquist plot for –800 to –1,050 mV/SCE was relatively volatile, and there may be a slight anodic dissolution.

The time-dependent changes of R_{ct} fitted from the EIS data at various cathodic potentials was studied. Generally, a higher R_{ct} indicates a lower corrosion rate of steel. At OCP, the R_{ct} increased and reached the maximum value after 4 days, and then decreased gradually. The initial increase of R_{ct} can be attributed to the production of biofilm and corrosion products that formed a protective film on the specimen surface. After 4 days, the number of active SRB increased rapidly and reached the maximum value at 7 days, which accelerated the corrosion of X65 steel. In addition, the integrity of the protective film may be degraded, thereby forming an active corrosion cell between the FeS film (cathode) and the nearby metal substrate (anode), which resulted in a rapid decrease of R_{ct}. However, in the case of the cathodic polarization, R_{ct} was increased when the polarization potential shifted negatively. The results were well matched with the cathodic protection theory mentioned in Evan's diagram; that is, the increase of protective potential increased the corrosion resistance. The R_{ct} with the highest increase was observed at –1,050 mV/SCE. It revealed that

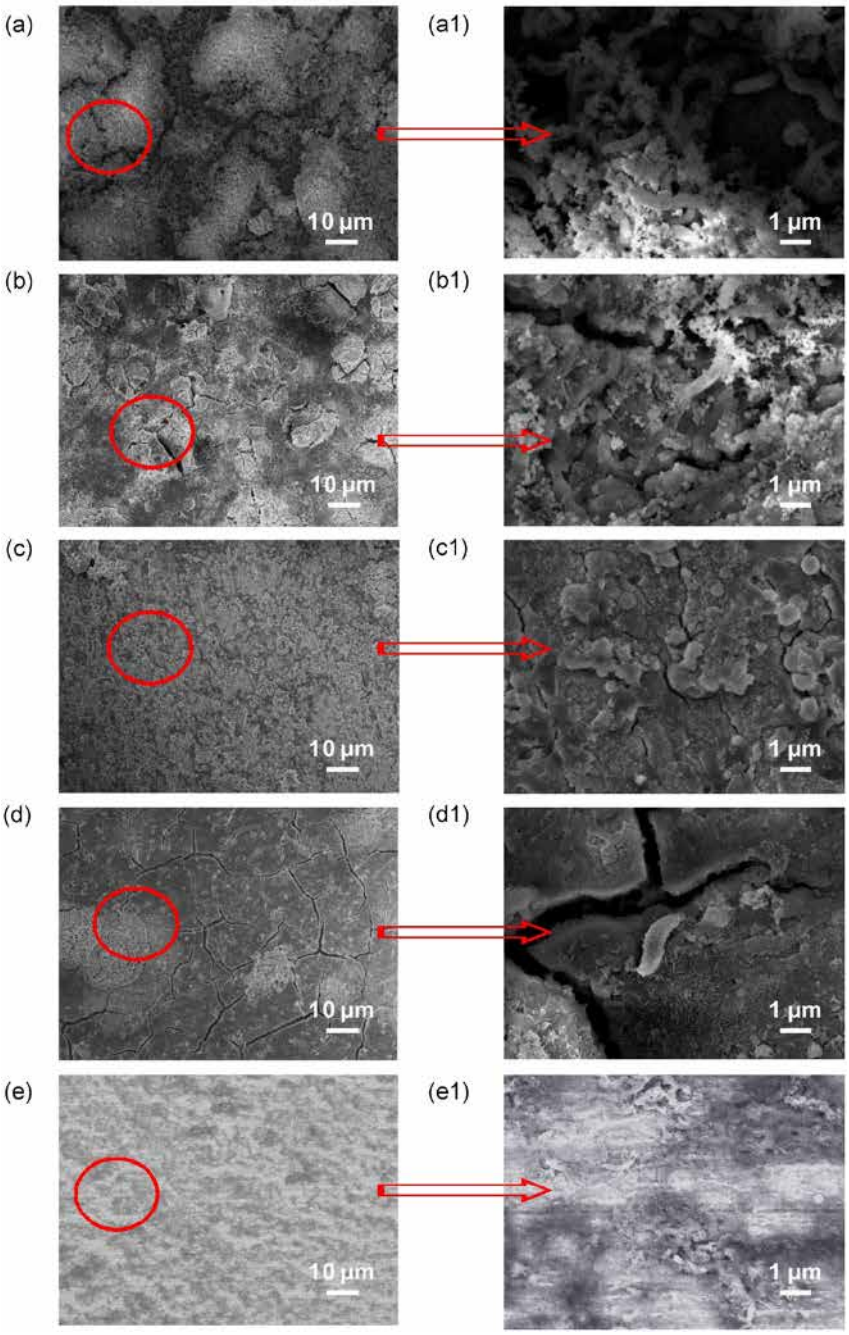

Figure 3: SEM images of X65 steel at various potentials: (a,a1) OCP; (b,b1) –800 mV/SCE; (c,c1) –1,050 mV/SCE; (d,d1) –1,050 to –800 mV/SCE, and (e,e1) –800 to –1,050 mV/SCE after 14 days of exposure in the SRB-containing medium. OCP, open circuit potential; SCE, saturated calomel electrode; SEM, scanning electron microscope; SRB, sulfate-reducing bacteria.

anodic dissolution was almost inhibited at the cathodic potential of –1,050 mV/SCE.

Current densities' recording

It was observed that the current density decreased rapidly within a few hours and reached a steady state. Additionally, the cathodic current increased after a few days. This increase was suggested to result from the following factors: (a) cathodically produced hydrogen promoted an SRB activity and (b) iron sulfides produced by SRB were cathodic, relative to X65 steel, which may form a corrosion cell, resulting in a higher cathodic current.[29]

pH variation

The pH values decreased abruptly in the SRB-containing culture solution with bacterial growth and then increased. The initial drop in pH values can be attributed to the generation of organic acids. SRB consumed cathodic hydrogen through a hydrogen intermediate (i.e., hydrogenase) for the reduction of SO_4^{2-}, as given below:

$$SO_4^{2-} + 8H^+ + 8e^- \rightarrow HS^- + 3H_2O + OH^- \quad (1)$$

The reaction increased the concentration of OH^- because it consumed H^+, increasing, the pH of the solution. Although the changes in pH for all systems exhibited a similar pattern, the pH values at various polarization potentials were higher than that at OCP. This indicated that the alkalinity generated by cathodic polarization was higher than that by microbiological activity.

Surface analysis

Figure 3 shows the SEM images of X65 specimens at various polarization potentials after 14 days of exposure in SRB-containing seawater. A large number of loosely discrete products were attached to the surface at OCP (**Figure 3a**). Numerous SRB cells were embedded in the corrosion products and biofilm matrix. The EDS results showed that the elements of corrosion products were mostly Fe, C, O, and S. Thus, the corrosion products were principally iron oxides, sulfides, as well as carbon-based compounds that accumulated from the culture medium. When the cathodic potential of –800 mV/SCE was applied on the electrode, the corrosion product layer was more compact (**Figure 3b**). It is observed that SRB cells still existed among the corrosion products. At –1,050 mV/SCE, dense deposits were formed on the X65 steel surface (**Figure 3c**) and no bacteria were observed on the surface. The EDS analysis indicated the presence of calcareous deposits and

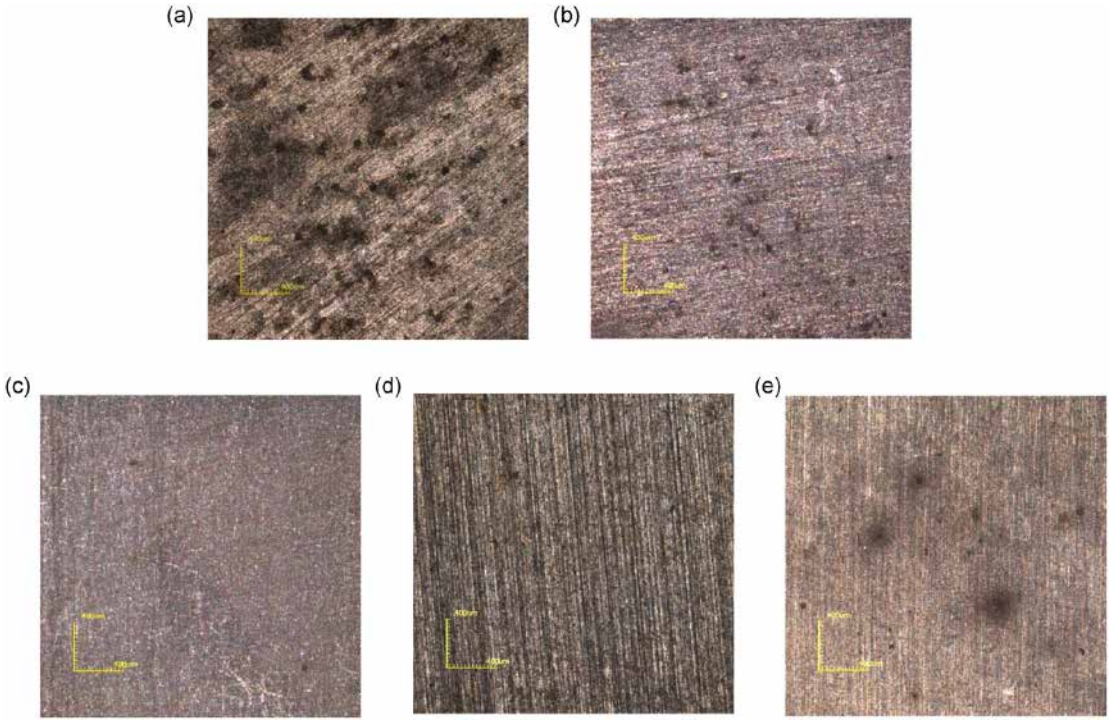

Figure 4: Corrosion morphologies of X65 steel after removing corrosion products at various potentials: (a) OCP; (b) –800 mV/SCE; (c) –1,050 mV/SCE; (d) –1,050 to –800 mV/SCE, and (e) –800 to –1,050 mV/SCE. OCP, open circuit potential; SCE, saturated calomel electrode.

a low amount of iron sulfides. The formation of calcareous deposits on the electrode surface was the result of negative protection potential producing high pH value, which was beneficial to the deposition of calcium ions. At –1,050 to –800 mV/SCE, there were obvious corrosion cracks on the surface, which were caused by drying during specimen preparation (**Figure 3d**). At –800 to –1,050mV/SCE, the steel electrode contained a layer of corrosion products (**Figure 3e**) with extensive SRB cells.

Corrosion morphologies of X65 steel after removing corrosion products are shown in **Figure 4**. Some big and deep pits were observed at OCP (**Figure 10a**), which was attributed to anodic dissolution occurring on the steel surface and SRB-induced pitting. At cathodic potential of –800 mV/SCE (**Figure 10b**), pitting corrosion still occurred. By contrast, the surface morphology of the specimen at –1,050 mV/SCE was, in general, smooth with no apparent pitting corrosion (**Figure 10c**). It was consistent with the electrochemical result that corrosion was prevented by a cathodic potential of –1,050 mV/SCE. At –1,050 to –800 mV/SCE (**Figure 4d**), the general corrosion of X65 steel was effectively controlled, except for a few small pits. When the cathodic potential shifted negatively from –800 to –1,050 mV/SCE, these pits seemed to be wider but not deeper than that at –800 mV/SCE (**Figure 4e**).

XPS analysis

XPS spectra were employed to qualitatively and quantitatively determinate the corrosion products of the X65 specimen. For the Fe spectrum of corrosion products, $FeSO_4$, Fe_2O_3, FeOOH, FeS, and FeS_2 were detected in almost all specimens. Interestingly, some iron sulfides were also found at the cathodic potential of –1,050 mV/SCE. It can be hypothesized that a negative potential of –1,050 mV/SCE can play a better protective effect, but it cannot completely eliminate the occurrence of MIC.

The influence of cathodic potential on SRB-induced corrosion

The SEM micrographs in this study showed a significant reduction of the bacterial number on the cathodic surface polarized to –1,050 mV/SCE. For most cathodic surfaces in the anaerobic condition, an impressed cathodic potential forced the following reactions:

$2H_2O + 2e^- \rightarrow H^+ + 2OH^-$. (2)

In this case, the production of OH^- caused an increase of interfacial pH, which seemed high enough to inhibit the initial attachment of SRB. Furthermore, the surface charge on bacteria cells depended on interfacial pH, which determined the degree of protonation of ionogenic groups associated with the cell wall to be negatively charged. The microbial cell produced a negatively charged polysaccharide, glycocalyx; thus, its attachment to the polarized surface was electrostatically repelled when a cathodic potential of –1,050 mV/SCE was applied.[30,31]

Calcareous deposits were formed on the surface of the cathodically polarized electrode. The increase in local pH, in turn, forced a shift in the equilibria of all chemical reactions involving calcium, magnesium, and carbonate:

$HCO^- + OH– \rightarrow H_2O + CO_3^{2-}$ (3)

$Mg^{2+} + 2OH^- \rightarrow Mg(OH)$ (4)

$Ca^{2+} + CO_3^{2-} \rightarrow CaCO_3$ (5)

Cations such as Ca^{2+} and Mg^{2+} are required for bacterial adhesion as a "bridge."[32] The precipitation of Ca and Mg ions caused a decrease in their local concentration due to the generation of OH^-, thereby inhibiting the attachment of SRB to the surface of cathodically polarized X65 steel. These calcareous deposits also provided a physical barrier to general corrosion attack. At the cathodic potential of –1,050 mV/SCE, the formation of calcareous deposits and the alkaline environment on the surface of the polarized electrode was not suitable for SRB to obtain electrons from the overly negative polarized X65 steel and grow. According to the corrosion morphology of X65 steel after removing corrosion products (**Figure 4c**), the protection potential of –1,050 mV/SCE was sufficient to control the corrosion induced by SRB.

The bacterial activity was not affected by the protection potential of –800 mV/SCE applied to the X65 steel. Besides the general corrosion observed on the metal surface, a type of localized corrosion was developed when the potential of –800 mV/SCE was applied to the SRB system (**Figure 4b**). Thus, –800 mV/SCE was not sufficient to inhibit SRB-induced corrosion. Some works have found that cathodic hydrogen generation at the cathodically protected surface promoted the growth of hydrogenase-containing SRB.[32] Chemical species (including H^+ ions) were reduced at the metal surface:

$H^+ + e^- \rightarrow {}^{[H]}$. (6)

The generated atoms $^{[H]}$ were transported to the biofilm and then oxidized by hydrogenase enzyme to reduce SO_4^{2-}. Further, H^+ protons were adsorbed on the metal surface and reduced again. It was apparent that the cathodic potential changed the bacterial metabolism and consequently affected the current demand.

However, several studies indicated that SRB can also obtain electrons from metallic iron directly via membrane-associated proteins (e.g., cytochromes) to reduce SO_4^{2-}.[33-35] Therefore, the cathodic polarization potential must be lower than the optimal protection criterion for steel due to the presence of SRB.

In the experiment conducted at the cathodic potential ranging from –800 to –1,050 mV/SCE, the SEM observation (**Figure 3e**) indicated that SRB strongly attached to the electrode surface, despite the fact that potential negatively shifted to –1,050 mV/SCE after 7 days. The reason was suggested that cathodic polarization was not sufficient to remove bacteria from the pre-existing biofilm.[29] When a potential of –1,050 to –800 mV/SCE was applied, the protective effect was similar to that at –1,050 mV/ SCE. It indicated that the changes in the metal interface caused by –1,050 mV/SCE were sufficient to suppress SRB-induced corrosion for a period of time after the potential shifted to –800 mV/SCE. However, long-term predictions require further research in SRB-containing seawater.

CONCLUSIONS

In this study, it was demonstrated that the degree of SRB attachment on the electrode surface was associated with the electric quantity and the intensity of the cathodic current. Due to the build-up of negative charges on the electrode surface, the cathodic current of 400mA/m2×30 hr effectively inhibited bacterial attachment. In contrast, when a low cathodic current of 100mA/m2 was applied, bacterial attachment and growth were promoted. Also, the attachment of SRB on the electrode surface was not inhibited by the potential of –800mV/SCE. The generated atoms [H] on the polarized surface contributed to the metabolic activity of SRB. A further negative shift

of the protection potential to –1,050mV/SCE exhibited an effective inhibitory effect on SRB-induced pitting corrosion. The impressed charges, the increase of pH, and the formation of calcareous deposits on the electrode surface were the driving forces to inhibit the attachment of SRB. The cathodic potential ranging from –1,050 to –800mV/SCE also provided effective protection for X65 steel due to the interfacial changes caused by potential of –1,050mV/SCE in the first 7 days. However, at the potential ranging from –800 to –1,050mV/SCE, pitting corrosion still existed on the electrode surface, indicating that the applied potential of –1,050mV/SCE could inhibit SRB attachment, but it was not sufficient to remove SRB from the pre-existing biofilm.

REFERENCES

[1] *Y. S. Kim, S. K. Lee, H. J. Chung, J. G. Kim, Ocean Eng. 2018, 148, 223.*

[2] *J. H. Kim, Y. S. Kim, J. G. Kim, Ocean Eng. 2016, 115, 149.*

[3] *R. G. Esquivel, G. Z. Olivares, M. J. H. Gayosso, A. G. Trejo, Mater. Corros. 2011, 62, 61.*

[4] *C. H. Williamson, L. A. Jain, B. Mishra, D. L. Olson, J. R. Spear, Appl. Microbiol. Biotechnol. 2015, 99, 6945.*

[5] *R. Javaherdashti, Appl. Microbiol. Biotechnol. 2011, 91, 1507.*

[6] *K. M. Moon, H. R. Cho, M. H. Lee, S. K. Shin, S. C. Koh, Met. Mater. Int. 2007, 13, 211.*

[7] *F. M. AlAbbas, R. Bhola, J. R. Spear, D. L. Olson, B. Mishra, Int. J. Electrochem. Sci. 2013, 8, 859.*

[8] *Y. Zhu, Y. Huang, C. Zheng, Q. Yu, Mater. Corros. 2007, 58, 447.*

[9] *S. Y. Li, K. S. Jeon, T. Y. Kang, Y. T. Kho, Y. G. Kim, Corrosion 2001, 57, 815.*

[10] *V. W. Kuehr, V. D. Vlugt, Water (den Haag) 1934, 18, 147.*

[11] *S. Daumas, M. Magot, J. L. Crolet, Res. Microbiol. 1993, 144, 327.*

[12] *D. Thierry, W. Sand Corrosion Mechanisms in Theory and Practice (Eds: P. Marcus, J. Oudar), Marcel Dekker, New York, NY 1995.*

[13] *D. Thierry, W. Sand Corrosion Mechanisms in Theory and Practice, 2nd ed. (Ed: P. Marcus), Marcel Dekker, New York, NY 2002.*

[14] *W. A. Hamilton, Biofouling 2003, 19, 65.*

[15] *R. Jia, J. L. Tan, P. Jin, D. J. Blackwood, D. Xu, T. Gu, Corros. Sci. 2018, 130, 1.*

[16] *T. Q. Wu, M. C. Yan, D. C. Zeng, J. Xu, C. K. Yu, C. Sun, W. Ke, Acta Metall. Sin. 2014, 28, 93.*

[17] *H. A. Videla, Biofouling 2009, 15, 37.*

[18] *P. Zhang, D. Xu, Y. Li, K. Yang, T. Gu, Bioelectrochemistry 2015, 101, 14.*

[19] *S. H. Hong, J. Jeong, S. Shim, H. Kang, S. Kwon, K. H. Ahn, J. Yoon, Biotechnol. Bioeng. 2008, 100, 379.*

[20] *O. Istanbullu, J. Babauta, H. Duc Nguyen, H. Beyenal, Biofouling 2012, 28, 769.*

[21] *S. Shim, S. H. Hong, Y. Tak, J. Yoon, Biofouling 2011, 27, 217.*

[22] *C. Sun, J. Xu, F. H. Wang, C. K. Yu, Mater. Corros. 2010, 61, 762.*

[23] *S. G. G. de Saravia, M. F. L. de Mele, H. A. Videla, R. G. J. Edyvean, Biofouling 1997, 11, 1.*

[24] *G. Olivares, G. Mejia, G. Caloca, I. Lopez, F. Dabur, C. Ulloa-Ochoa, R. Esquivel, Corrosion 2003.*

[25] *T. Liu, Y. F. Cheng, J. Alloy. Compd. 2017, 729, 180.*

[26] *W. W. Wilson, M. M. Wade, S. C. Holman, F. R. Champlin, J. Microbiol. Methods 2001, 43, 153.*

[27] *A. T. Poortinga, J. Smit, H. C. V. D. Mei, H. J. Busscher, Biotechnol. Bioeng. 2001, 76, 395.*

[28] *F. Guan, X. Zhai, J. Duan, M. Zhang, B. Hou, PLOS One 2016, 11, e0162315.*

[29] *J. G. Guezennec, Int. Biodeterior. Biodegrad. 1994, 34, 275.*

[30] *B. Little, P. Wagner, D. Duquette, Corrosion 1988, 44, 270.*

[31] *R. G. J. Edyvean, A. D. Maines, C. J. Hutchinson, N. J. Silk, L. V. Evans, Int. Biodeterior. Biodegrad. 1992, 29, 251.*

[32] *J. Guezennec, Biofouling 1991, 3, 339.*

[33] *J. Duan, S. Wu, X. Zhang, G. Huang, M. Du, B. Hou, Electrochim. Acta 2008, 54, 22.*

[34] *H. Venzlaff, D. Enning, J. Srinivasan, K. J. J. Mayrhofer, A. W. Hassel, F. Widdel, M. Stratmann, Corros. Sci. 2013, 66, 88.*

[35] *H. T. Dinh, J. Kuever, M. Mußmann, A. W. Hassel, M. Stratmann, F. Widdel, Nature 2004, 427, 829.*

Copyright:
10.1002/maco.202011715
M. Lv, X. Li, M. Du
Materials and Corrosion;

03 Comparison of test methods used to analyze stress corrosion cracking of differently tempered 7xxx alloys

N. Magaji, R. Mayrhofer, B. Krger, *et al.*

ABSTRACT

This paper compares and critically analyzes various test methods used to assess stress corrosion cracking (SCC) susceptibility of the alloy EN AW-7075 (Al-Zn-Mg-Cu) in various temper conditions. Constant load test in an alternating immersion environment was used as the standard reference test. Constant displacement tests in the form of U-bend specimens and four-point loaded bend specimens was conducted in a neutral and acidic salt-spray fog test environment, an alternating salt spray fog environment, and alternating immersion environment. A novel incremental step load test was also carried out in a continuous immersion environment. It was shown that the neutral salt-spray fog test environments could potentially substitute the alternating immersion test for testing SCC susceptibility.

INTRODUCTION

The high-strength Al-Zn-Mg-Cu alloys (7xxx series) have drawn considerable attention in the automobile industry in the past few years. This is due to their high strength (up to 600 MPa), light weight, and high resistance to corrosion.[1] However, one of the main problems is their high risk of susceptibility to stress corrosion cracking (SCC), which can lead to catastrophic failures in service.[2] Due to the complex nature of SCC, there is currently no common consensus on possible mechanisms.[3,4] SCC is highly influenced by the nature and magnitude of stress. Consequently, the choice of loading systems for testing SCC can have a substantial impact on the test results.[5] The three commonly used stressing modes involve the application of a constant total strain, a constant load, and the use of a constant strain rate.

The aim of this work is to compare and critically analyze the advantages and disadvantages of the most common SCC test methods for the assessment of SCC in high-strength Al-Mg-

Zn-Cu alloys. This work aims to understand the practicality of each test method with respect to automotive applications and analyze the influencing parameters that need to be considered when choosing an appropriate test method.

MATERIALS AND METHODS

Materials

The material, whose composition is given in **Table 1**, was received in 300 × 300 $mm^{[2]}$ sheets of 1.5 mm thickness in three heat treatment conditions (**Table 2**).

Corrosion testing

Constant load test

The constant load test was carried out according to ASTM G47-98.[6] Standard A80 samples according to DIN EN ISO-6892-1:2017–02 were prepared by punching,[7] and they were uniaxially stressed to maintain a constant load corresponding to 75% of their yield strength.[6] Each stressed sample was subjected to alternating immersion testing in an aqueous NaCl solution according to ASTM G44-99 for a total duration of 30 days. A minimum of three trials were carried out for each material. The main analysis parameter considered was the time to failure. Fracture surfaces were analyzed using a scanning electron microscope to determine the nature of fracture. In addition, optical microscopy was carried out on fractured and unfractured samples.

U-bend test

The U-bend sample preparation was performed according to ASTM G30-97.[8] U-bending samples were punched with an impact cutter and holes were drilled on either side. Spacers were used to ensure that bending did not exceed the final bend that was fastened. Once the samples were prepared, they were exposed to five environments for a definite period, or until failure of the sample. See **Table 3** for details.

Four-point loaded bend test

The four-point loaded specimens were prepared according to ASTM G39-99.[9] Four-point bending specimen holders support the specimen at the ends and bend the specimens by forcing two inner supports against it. Once the samples were prepared, a minimum of three samples were exposed to two test environments, namely DIN EN ISO 11997- 1 Cycle B and ASTM G44-99 (Alternating immersion test).[10,11] The main analysis parameter considered was the time to failure. SEM fractographic analysis of the failed samples was carried out to determine the nature of the fracture.

Incremental step load test

In this test, specimens were subjected to an increasing step load cycle while being exposed to a test environment. The maximum load reached was used to compare the susceptibility of different alloys. One of the principal advantages of this test is that it always ends with a failure and does not need to be stopped after a specific duration. The setup of this experiment is similar to that of a constant load test, wherein an A80 sample is covered by a solution holder and uniaxially stressed. The test starts with a pre-load time of 96 h, in which the load is set to 50% of maximum load (load to failure). Thereafter, the load is increased every hour in steps of 5% of maximum force until the specimens fail. Throughout this load cycle, the sample is exposed to a test solution of 5% NaCl with an initial pH of 4, achieved by adding HCl to the solution. The minimum load to failure was compared to determine the SCC susceptibility ranking. SEM investigations as well as optical microscopy were carried out to determine the nature of the fracture surface.

Table 1: Composition of the test material (wt%)

Si	Mg	Mn	Cu	Fe	Zn	Cr	Ni	Zr	Al
0.07	2.43	0.05	1.58	0.16	5.94	0.21	0.01	0.02	Bal.

Table 2: Temper treatment cycles

Temper treatment	Tempering process
T4	As delivered
T6	T4+ 130 °C for 13 h
T7	T4 + 115 °C for 6 h + 168 °C for 16 h

Environment	Temperature	Description	Solution concentration	pH	Maximum exposure duration
DIN EN ISO 11997–1:2016-5	Cyclic as shown in Fig.	Cyclic Humidity	5 wt% NaCl	6.5–7.2	42 days
DIN EN ISO 9227:2012 NSS	35 ± 2 °C	Continuous spray	5 wt% NaCl	6.5–7.2	30 days
DIN EN ISO 9227:2012 CASS	50 ± 2 °C	Continuous spray	5 wt% NaCl + 0.26 g L^{-1} of ($CuCl_2.2H_2O$)	3.1–3.3	14 days
ASTM G44-99	Solution:23 ± 2 °C	Alternating immersion	3.5% NaCl	6.5–7.5	30 days
	Air: 23 ± 2 °C (anomaly from the norm which states 27 ± 2 °C)				
DIN 55665:2007–01 (Outdoor Exposure Test)	Natural weather conditions	Weekly spray	3% NaCl solution	6.5–7.5	1 year

Table 3: Description of environments used in this study

Analytical methods

Optical microscopy

After the test exposure duration, the samples were cleaned, and cross-sections of each specimen type were prepared. These micro-sections were observed to determine the nature of the crack, the influence of other corrosion forms, and crack initiation sites. The microscopy was done using an Olympus® LEXT™ OLS4100 laser scanning digital microscope. The samples for each microstructural analysis were hot mounted under pressure with an epoxide resin. Subsequently, they were ground to 1200 level grit and then polished. The etching of the samples was carried out by dipping the specimen in 10% phosphoric acid for 30 min.

Scanning electron microscopy

Fracture analysis of failed specimens was performed using a scanning electron microscope (SEM) to determine the mode of failure and the nature of the fracture surface. The electron microscopy was performed with the MIRA Scan 3, from Tescan. A 10 V accelerating voltage was used for secondary electrons imaging.

RESULTS AND DISCUSSION

Characterization of materials

As expected, the T6 tempered alloy had the highest ultimate tensile strength and hardness. The electrical conductivity was seen to increase with annealing duration.

Constant load test

The constant load test was used as a standard reference for this study due to the experience and knowledge base in this test.

The results of the minimum time to failure for the constant load test, showed a clear influence of the temper treatment on the SCC susceptibility, with 7075-T4 being the most susceptible material, since it showed the fastest failure within 2 days of testing, followed by 7075-T6, which failed after 5 days of testing. The 7075-T7 alloy passed the 30-day test limit without failure.

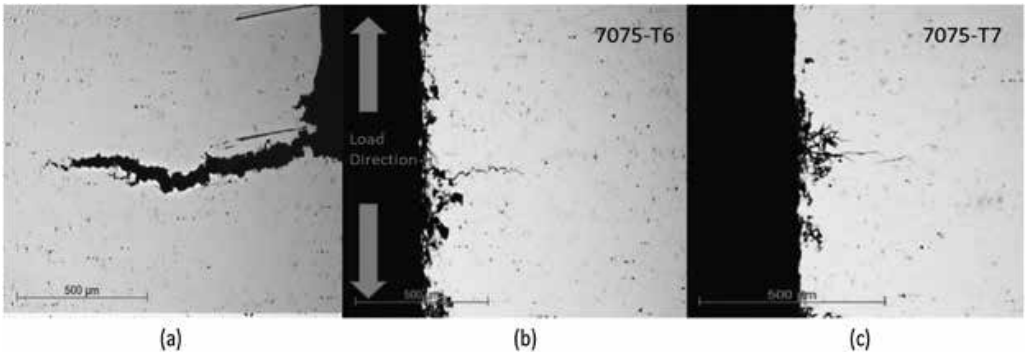

Figure 1: Cross-sections of the constant load specimens observed under optical microscopy. (a) 7075-T4, (b)7075-T6, and (c) 7075-T7

The metallographic examination of failed specimens revealed that the nature of the cracks was intergranular and multiple cracks were observed near the surface of the failure. **Figure 1** shows the cross-section of the tested specimen. While 7075-T4 and 7075-T6 show localized corrosion influence, the 7075-T7 alloy shows crack initiation from an intergranular corrosion site.

Moreover, the SEM fractography of tensile tested samples in air revealed a ductile fracture surface with a typical honey-comb structure. In comparison, the fracture surface of the sample that failed during the SCC test showed an intergranular fracture surface, which is mostly brittle in nature. Primary cracks along with secondary branching are also visible on the surface. The failed sample of 7075-T6 alloy also showed a similar fracture surface, with a brittle quasi cleavage structure with primarily intergranular fracture surface.

These results indicate that the failure mechanism is intergranular in nature and correlate well with investigations by Schnatterer and Zander,[12] who got the same ranking of susceptibility using the SSRT test. They attributed the higher SCC susceptibility of 7075-T4 to the substantial IGC influence, due to anodic dissolution of the MgZn2 precipitates and lower SCC susceptibility of the over-aged alloy to incorporation of Cu to the grain boundary precipitates, resulting in an increase of their potential. Speidel *et al*.[5] also observed that over-aging (T7) greatly decreases the SCC susceptibility of high copper containing alloy, attributing it to formation of nobler Cu containing precipitates and, therefore, reducing anodic dissolution. However, a deeper understanding of this mechanism can only be obtained through TEM observations and grain boundary studies of the materials and the effect of tempering.

U-bend test

The 7075-T4 alloy underwent the earliest failure in all the corrosive environments as in the constant load test. It failed within a span of two days in all the considered environments. The failures of 7075-T6 were slightly delayed compared to the T4-treated samples in all the environments. The longest time observed for failure of this material was found for the alternating immersion test of 15 days. The 7075-T7 alloy showed no complete failure after the maximum duration of tests. However, it must be noted that samples of this temper from the alternating immersion test and the CASS test showed micro-cracks in optical microscopy.

The output of these results has direct correlation with the standard reference test. Comparing the time to failure of alloys in the different environments, the ranking of susceptibility is the same in all the environments. Interestingly, the correlation of the ranking produced by the fog tests, to the outdoor exposure test is also substantial. This good correlation of the climate tests to the outdoor exposure test shows a potential for the use of climate-chamber tests, which are a common practice test in automotive corrosion testing. The salt spray tests could be further developed to test SCC and potentially replace the alternating immersion test.

The DIN EN ISO 9227–2012 CASS test shows the highest corrosion influence of the four environments tested. This could be due to its acidic nature, higher temperature, the presence of higher chloride ions (due to presence

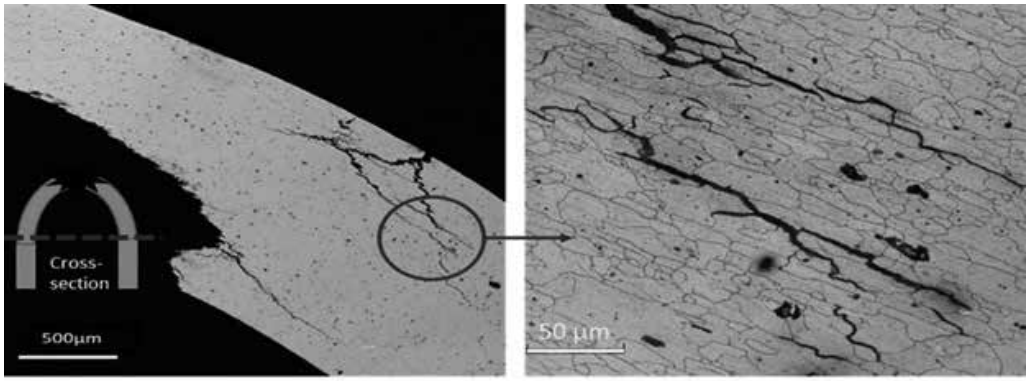

Figure 2: (a) Failed 7075-T4 sample after 1 day of exposure to the DIN EN ISO 9227:2012 NSS environment and (b) etched and magnified image showing intergranular fracture.

of copper chloride), and due to the localized galvanic corrosion by copper ions. However, it is noticed in the micrographs and SEM fractographs that stress corrosion cracking, in this environment, is accompanied by severe forms of corrosion, especially intergranular corrosion. This makes it difficult to determine the exact cause of failure, deeming this environment inappropriate to test SCC.

Figure 2a shows the crack surface of the 7075-T4 alloy after 2 days of exposure to the neutral salt spray environment (DIN EN ISO 9227-2012 NSS). It represents the typical crack propagation direction observed in all the failed samples. Branching of the crack surface and multiple cracks are visible.

These cracks could also possibly be initiated before the cracks that led to failure. Hence, multiple cracks could lead to a significant relaxation of stress as compared to one propagating crack, leading to slower crack propagation and crack arrest. It can also be seen from the etched sample (**Figure 2b**) that the crack propagation is intergranular in nature. This factor could influence the results, while considering time to failure as primary criteria to qualify materials.

It is also observed that the crack initiates perpendicular to the surface and on further propagation changes its direction to parallel to the upper surface and arrests within the sample before failure. The U-bend sample has uneven stress distributions within the sample due to its high plasticity. Once a crack initiates in these regions, the stress distribution in the U-bend sample changes. The stress direction could also change, hence changing the crack path as well. This uneven change in stress distribution is an important factor to be considered in SCC testing.

Four-point loaded bend specimen

A comparison of the results of this test with the reference test, both in an alternating immersion environment, gives a clear difference in the effect of loading mode, since they were both stressed to 75% of the yield strength and exposed to the same environmental condition. The 7075-T6 alloy, in the constant load test, showed earliest failure after 5 days of exposure, whereas the same alloy in the four-point load bending test did not fail within 30 days of exposure. This could be attributed to the stress relaxation that occurs in the four-point load test on the initiation of the crack on the edges. On the other hand, crack initiation in the constant load test leads to the increase of stress on the remaining sample, leading to faster propagation of cracks and faster failure. This result agrees with the results of Brenner et. al. who also attributed the faster failure of the constant load test to stress concentration.[13]

During the four-point bending test, we observed that the failure crack was in the contact region of the roller and the specimen, rather than the expected region of the sample between the contact rollers where the stress is distributed. There are two possible factors for this behavior or the combination of both, that results in this cracking. The first factor is the frictional stress at the point of contact of the roller and the specimen as explained by Turnbull *et al*.[14] This failure adds unknown stresses to the induced stresses in the specimen. This error on the stress invalidates the advantage of knowing the exact stress to fail-

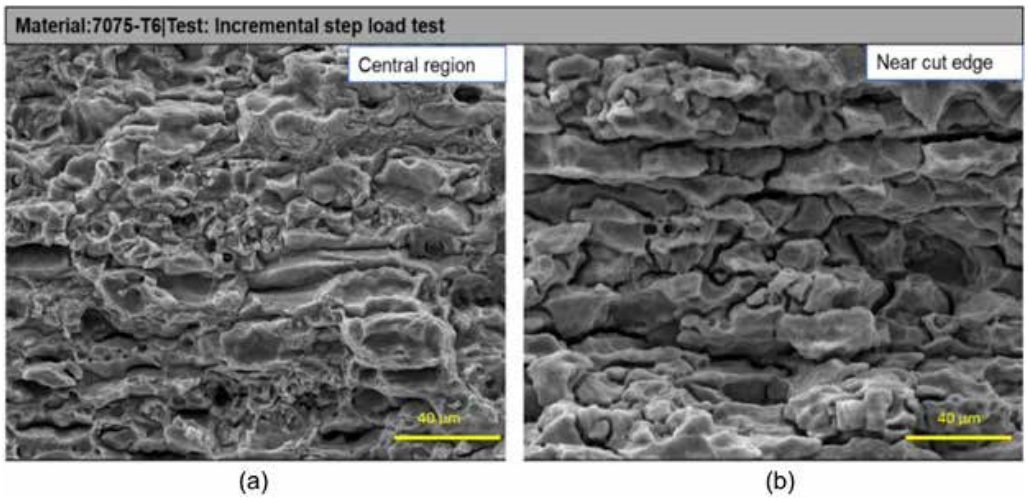

Figure 3: 7075-T6 fracture surface after failure at 55% Fmk in the incremental step load test. (a) Center of the cross section and (b) near the cut edge of specimen.

ure in this type of specimen. The second factor is the crevice corrosion that could take place at the contact point as mentioned in ASTM G39-99.[9] This crevice corrosion near the contact point is accompanied by an increase in hydrogen contents possibly leading to hydrogen included failure in this region. Since this is an uncontrolled process, it could lead to hindrance of the testing of SCC, and it becomes difficult to ascertain the parameters to failure.

Incremental step load test

The incremental step-load test is a novel test used in this study for testing the susceptibility of stress corrosion cracking of aluminum 7xxx alloys. The advantages of this test include the shorter timespan of the experiment of a maximum of 106 h, as compared to the other tests that ran up to 30 days or more. Another huge advantage of this test, as with the slow strain rate test, is that the test ends with failure for all the samples and does not need to be stopped at any arbitrary time, eliminating the uncertainty of whether the time ascertained for the test is appropriate. Although a practical application of incremental loading of stress may not be reasonable in real-world conditions, this test could be suitable for qualitative comparison of susceptibility of alloys by two factors, namely time to failure and maximum stress withstood. This gives a good qualitative ranking capability when alloys are to be compared. In this work, the results of the incremental step load test showed good agreement with the standard reference test.

The proposed mechanism taking place in this test is comparable to that of SSRT. Since SCC is a time dependent process, the aim of the preload time, in which the sample is exposed to the corrosive 5% NaCl solution and stressed at a load of 50% of the ultimate tensile strength, is to initiate stress corrosion cracking in the material, assuming that the stress is sufficient to do so. Once the crack is initiated after the pre-load time, the stress is increased and held in that stress state for a given time. The aim of this hold time is to induce SCC within the opened regions of crack, as in the slow strain rate test, producing then a complete brittle fracture. Since this is a load-driven test, the initiation of a crack would result in the increase of stress in the remaining specimen. This could lead to plasticity in the remaining region, hence, leading to a higher probability of stress corrosion cracking to occur. If the hydrogen induction mechanism is taken into consideration, the hydrogen atoms have time to be adsorbed into the open crack surface, and an increase of stress could increase the movement of hydrogen within the material by movement of dislocations. This induction of SCC would then differ with difference in susceptibility of materials, leading to failure of more susceptible alloys at lower stresses and vice versa, thus creating a ranking of the alloys.

The incremental step-load test considers two parameters to determine susceptibility of the alloy, namely the maximum stress withstood for the step loading and the time to failure. The 7075-T4 did not withstand the preexposure duration and failed after 48 h of expo-

sure to 5% NaCl with a stress of 50% of the maximum load to failure (Fmk) followed by the failure of 7075-T6 at 63 h. The minimum load to failure ranged from 50% to 85%. The over-aged alloy did not show any susceptibility and passed the maximum load step of 95% Fmk. It is interesting to note, the correlation between these results to the other tests and the similarity of the ranking of the materials.

Figure 3 shows the fracture surface of 7075-T6 which failed at a stress of 55% Fmk, where Fmk stands for maximum load to failure. Two regions, one at the center of the specimen cross-section and another near the cut edge, show very different morphologies. The former shows both brittle and ductile areas. The region near the cut edge, however, shows a complete brittle intergranular cracking with branching. This difference in morphology could be attributed to the stresses present at the edges due to cutting. This could also explain the difference in failure stresses ranging from 50% Fmk to 85% Fmk. The embrittlement near the edges could be due to the effect of the plastic deformation of the edges due to punching, which causes substantial residual stresses on the specimen. The initiation of cracks due to this, could be uneven depending on the cut edges and these cracks could result in an overload on the rest of the material, once the crack is initiated from the edge. This explains the ductile regions visible in the center of the fracture specimen. In order to reduce the effect of cut edges, it is proposed that the test be optimized by use of milled or lasered specimens.

Critical analysis of the test methods

This work demonstrates the importance of loading mode and magnitude during SCC testing. Two specimens in constant total strain mode were examined: U-bend and 4-point loaded bend specimen. It was seen that the plastically strained U-bend test showed fast results as compared to the elastically 4-point bend test, due to a higher magnitude of stresses. However, the disadvantage of plastic straining is the complex calculation of stresses within the sample and uneven distribution of stresses. This inhomogeneous stress distribution does not allow for a quantitative determination of threshold stresses for SCC failure. It must also be considered that elastically strained specimens undergo stress relaxation once the crack initiates. The extent of this relaxation is dependent on the sample holder and the specimen size.[15]

On comparison of constant load and constant strain mode, the stress concentration increases, in a constant load mode, once the crack initiates. This makes the constant load test a more severe test. Multiple cracks were also observed in failed specimens, which could lead to inhomogeneous stress relaxation.[16] All the environments tested in this work were found to be sufficiently aggressive to cause SCC. The same susceptibility ranking was obtained in all the environments and the outdoor exposure test. However, each environment had different speeds of failure. The slowest was the alternating immersion test, which could be explained by absence of free atmospheric hydrogen ions present in the test, as compared to the salt spray fog test. The severest test was the CASS test, which could be attributed to its low pH, high temperature, higher chloride ions, and presence of Cu2+ ions, which could lead to localized galvanic corrosion. However, optical microscopy showed, that this test was highly influenced by other corrosion forms, such as intergranular and pitting corrosion. These other corrosion forms could have a substantial influence on the time to failure as well, making it an inappropriate test method to test SCC. A detailed analysis of the influence of pH, salt-content, temperature, and other environmental factors needs to be carried out in order to develop an appropriate SCC testing environment.

CONCLUSIONS

Four tests were conducted, compared, and critically analyzed to determine an SCC susceptibility ranking for differently tempered 7075 alloys. The following is a summary of the important observations and results obtained in this work.

1. Comparison of various environments used in this thesis showed that the acidic DIN EN ISO 9227:2012 CASS environment had the strongest corrosion influence on the tested materials. However, the SCC was also accompanied by other forms of corrosion, which could possibly affect the test results. The results of salt-spray tests, DIN EN ISO 9227:2012 NSS and DIN EN ISO 11997-1(B), showed that these tests can be appropriate substitutes for the standard alternating immersion environment. Since these test environments are well established in the automotive application, they have the potential to be further used for testing SCC susceptibility of 7xxx alloys for automotive application.

2. The U-bend test was easy to execute and economically viable. It also exhibited a good qualitative differentiability of SCC susceptibility of the 7075 alloy to SCC, which was confirmed by the correlation to the reference test as well as the outdoor exposure test.

3. The U-bend test showed fast results due to the large plastic strains on the specimen, hence, it is appropriate for an accelerated qualitative test. However, influence of stress relaxation and stress-redistribution due to crack formation must be thoroughly analyzed to use this test for commercial applications.

4. The U-bend test also shows a large dependence on sample preparation.

5. The four-point loaded bend samples did not produce a good differentiability of SCC susceptibility within the timeframe of the test. This was attributed to stress relaxation of the specimen on crack formation. Moreover, the failure of specimens was partly associated with crevice corrosion and frictional stress at the point of contact of the metal and stressing frame. These factors must be taken into consideration for further application of this test method. Possible improvements in this test could include concentration of the stress in the center of the specimen by means of notching or punching.

6. With the present parameters of the incremental step load test, it was seen that it was difficult to determine the cause of failure in this test. The test parameters were seen to have a substantial influence on the result. The optimization of the parameters, such as pre-load timing, step duration, different environmental parameters, and mill finished edges, could be beneficial for the future use of this method as an accelerated test for SCC susceptibility of 7xxx alloys.

7. The naturally aged 7075-T4 alloy showed the highest susceptibility in all the tests, followed by the peak-aged 7075-T6 alloy. The over-aged 7075-T7 alloy showed reduced susceptibility.

REFERENCES

[1] *Davis, J. R. Corrosion of Aluminum and Aluminum Alloys. (ASM International, 1999).*

[2] *Raja, V. S. & Shoji, T. Stress Corrosion Cracking: Theory and Practice. (Elsevier Science, 2011).*

[3] *Marichev, V. A. The mechanisms of crack growth in stress corrosion cracking of aluminium alloys. Mater. Corros. und Korrosion 34, 300–309 (1983).*

[4] *Burleigh, T. D. The Postulated Mechanisms for Stress Corrosion Cracking of Aluminum Alloys: A Review of the Literature 1980-1989. CORROSION 47, 89–98 (1991).*

[5] *Speidel, M. O. Stress corrosion cracking of aluminum alloys. Metall. Trans. A 6, 631–651 (1975).*

[6] *ASTM G47-98(2011). Standard Test Method for Determining Susceptibility to Stress Corrosion Cracking of 2xxx and 7xxx Aluminium Alloy Products. (1998) doi:10.1520/G0047-20.*

[7] *DIN EN ISO 6892–1:2017–02. Metallische Werkstoffe- Zugversuch- Teil 1. Prüfverfahren bei Raumtemperatur. (2017).*

[8] *ASTM G30-97(2016). Standard Practice for Making and Using Ubend Stress-Corrosion Test Specimens. (1997).*

[9] *ASTM G39-99 (Reapproved 2016). Standard Practice for Preparation and Use of Bent-Beam Stress-Corrosion Test Specimens. (1999).*

[10] *ASTM G44-99 (Reapproved 2013). Standard Practice for Exposure of Metals and Alloys by Alternate Immersion in Neutral 3.5% Sodium Chloride Solution. (1999).*

[11] *DIN EN ISO 11997-1:2016-05. Beschichtungsstoffe-Bestimmung der Beständigkeit (Salzsprühnebel)/trocken/feuchte. (2016).*

[12] *Schnatterer, C. & Zander, D. Influence of heat treatments on the stress corrosion cracking susceptibility of 7075 aluminum wires in NaCl solutions. Mater. Corros. 67, 1164–1172 (2016).*

[13] *Brenner, P. & Gruhl, W. No Title. Z. Met. 52, 599 (1961).*

[14] *Turnbull, A. & Crocker, L. E. Four point bend testing - finite element analysis of the stress and strain distribution. http://eprintspublications.npl.co.uk/6097/ (2014).*

[15] *Turnbull, A. Test methods for environment assisted cracking. Br. Corros. J. 27, 271–289 (1992).*

[16] *Richardson, T. J. A. Shreir's Corrosion. (Elsevier Science, 2009).*

04 Microstructure analysis of corrosion resistance of cast AlCu4Mg1 alloy

I. Hren, S. Kusmierczak, K. Kurajdov

ABSTRACT

In the automotive industry, the demand for aluminium alloys is growing every year and the requirements for these alloys are also increasing. This article discusses the evaluation of corrosion resistance of cast rods from alloy EN AW 2024. Experimental samples were laboratory subjected to a standard corrosion test according to CSN ISO 4287. Corrosive behavior was evaluated using light and electron microscopy. Furthermore, an analysis of the hardness of the material and the chemical composition was carried out. A map of corrosion-affected phases of the microstructure was also created, depending on time. This, together with the course of hardness, provides a comprehensive overview of the corrosion behavior of cast rods, which will serve as a starting point for further research in the field of barrier protection.

INTRODUCTION

The use of aluminum alloys in aerospace and automotive engineering products places increased demands on the corrosion resistance of materials to improve operational reliability and extend product life. The exclusion of possible causes of accidents and failures of automotive equipment (AE) due to the corrosion of aluminum alloys is based on comprehensive studies of climatic resistance of materials in their development and certification phase, rational design of AE products, excluding stagnant zones, as well as controlled operation, accompanied by timely identification and elimination of emerging corrosion damage.

Commonly used methods for assessing the corrosion status of an AE product are visual inspection and nondestructive testing. For aluminum alloys, the formation of pitting (PC) and intergranular corrosion (IC) is the most critical. Pitting corrosion develops mainly in the direction of maximum deformation and is accompanied by peeling of individual metal particles so that it can be detected visually without the use of instrumental research methods. On the other hand, IC, in which destruction

occurs along the grain boundaries deep into the semi-finished product, cannot be detected by the naked eye, so nondestructive methods are required. Not much work has been done to study the effect of the degree of sensitivity of alloys on MCC and the change in their mechanical properties after casting.

There is a need to study the influence of IC in climatic tests of structural aluminum alloys operating in conditions of increased aggressiveness of the atmosphere to change mechanical properties, which is necessary for the development of preventive measures aimed at improving reliable car operation. The aim of the article is to investigate the corrosion behavior of aluminum alloy 2024 in a salt environment with respect to the surface condition of the corrosion product in the alloy.

RESEARCH MATERIAL AND METHODS

The composition of the alloy 2024[1] is given in **Table 1**. Macro-photographies of obtained samples were registered using a Canon EOS 1200D camera. Metallographic specimens were prepared by grinding on waterproof abrasive papers (P180, P320, P600, P1200, and P2000) and polishing using water suspensions of polycrystalline diamond with grain size of 3 and 1 µm. Microstructural investigation was performed by means of light microscopy (Olympus® LEXT™ OLS5000 3D measuring laser microscope with 4K scanning technology and Olympus MXU software). A Tescan VEGA3 electron microscope was used to examine the microstructure of the alloy by SEM. The chemical composition of selected phases precipitated in the microstructure was analyzed by energy dispersive X-ray spectroscopy (EDX) using an analyzer and SW Esprit 1.9. The Vickers hardness of the material according to the standard ČSN 42 0374 was measured at a load of 0.025 kgf.

Si	Fe	Cu	Mn	Mg	Cr	Zn	Ti	Al
0.54	0.4	3.75	0.6	0.5	0.05	0.11	0.028	rest

Table 1: Chemical composition of EN AW 2024 alloy

RESULTS AND DISCUSSION

Microstructure analysis

The microstructure of the cast material (**Fig. 1**) consists of dendrites, which have a uniform distribution and comparable size. There is a clear occurrence of interdendritic porosity, which is typical for this type of Al alloy.[1–5] The microstructure of the experimental alloy EN AW 2024 in the cast state consists mainly of binary eutectic $\alpha + CuAl_2$ and a small amount of ternary eutectic $\alpha + CuAl_2 + Cu_2Mg_2Al_5$.

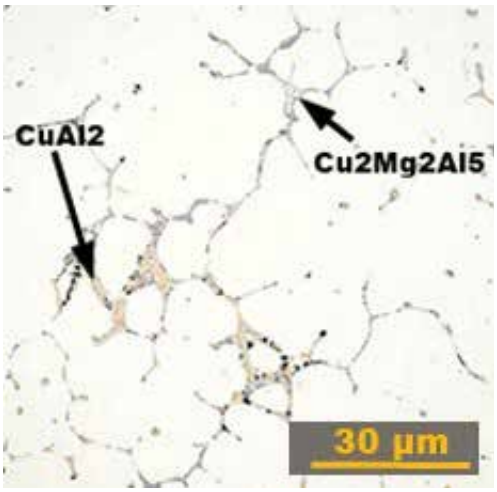

Figure 1: Microstructure of alloy AA 2024 with identified phase; mag. 500x.

MICROSCOPIC EVALUATION OF CORROSION ATTACK ON THE ALLOY

A salt spray test was performed according to CSN 038137. The samples were exposed to corrosion in a Liebisch S400 MTR corrosion chamber for the time specified in CSN ISO 8407.[6] The test was graded with exposure times of 168, 240, 480, and 720 hours. The individual cycles were performed in a test medium of 5% NaCl, concentration 50 g / l, at a temperature of 35 ± 20 °C (95 + 68 °F), and the pH of the solution was 6.5 to 7.2. The exposure time and labeling of the samples are given in **Table 2**.

At the end of the test, the samples were removed for corrosion, cleaned, dried, and metallographically prepared. Evaluation of corrosion attack was performed using a light microscope.

Corrosion load time	168 hours	240 hours	480 hours	720 hours
Sample identification	A	B	C	D

Table 2: Marking of EN AW 2024 alloy samples after corrosion test

After 168 hours of exposure in a corrosive environment (**Fig. 2**), uneven local areas of corrosion attack were visible in cross section. The microscope images indicated it was pitting corrosion. The pits were relatively large, such as the documented corrosion degradation: length 16.44 µm and depth of the pit 6.22 µm. The detail documents the state of grain boundaries in the subsurface layers of the experimental sample.

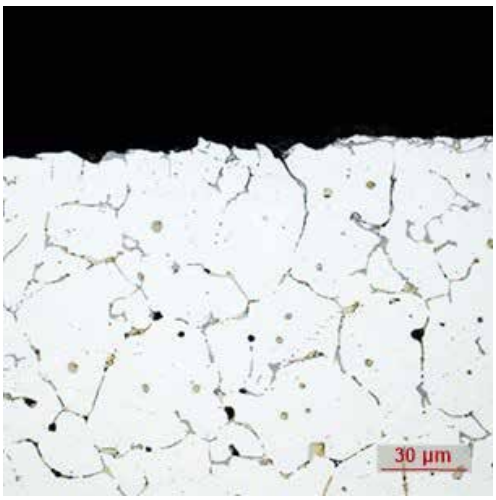

Figure 2: Corrosion attack, exposure in a corrosive environment; 168 h.

After 240 hours of exposure in a corrosive environment (**Fig. 3**), significant pitting corrosion in the sample can be seen, while with the time of exposure in the corrosive environment, the pitting grows unevenly (e.g., width 21.083 µm and depth 8.19 µm). There is also a significant weakening of grain boundaries by corrosion products in subsurface layers.

After longer exposure times, the corrosion attack spread in all directions. For clarity, **Figure 4** shows examples of pitting corrosion and the formation and spread of IC after only 480 hours of exposure in a corrosive environment. **Figure 4** shows the exclusion of phases along grain boundaries and interdendritic porosity at grain boundaries. In this case, the corrosion products penetrate to a depth of 75 µm from the sample surface. The detail documents the violation of the cohesion of the material.

After 720 h of exposure of the sample to a corrosive environment, intergranular corrosion spreads in all directions, which is shown in **Fig. 5**. The exclusion of Al_2Cu phases along grain boundaries is evident here. Intergranular corrosion penetrates up to 95 µm below the alloy surface.

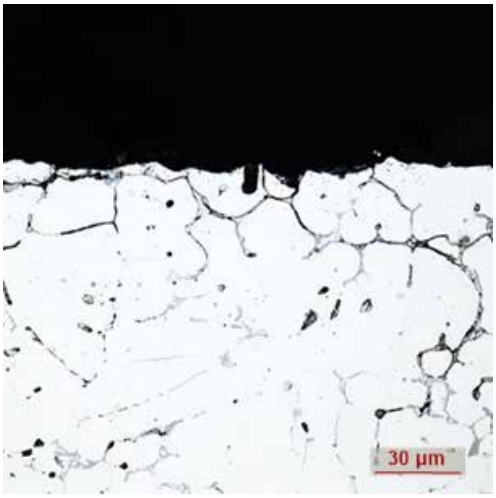

Figure 3: Corrosion attack, exposure in a corrosive environment; 240 h.

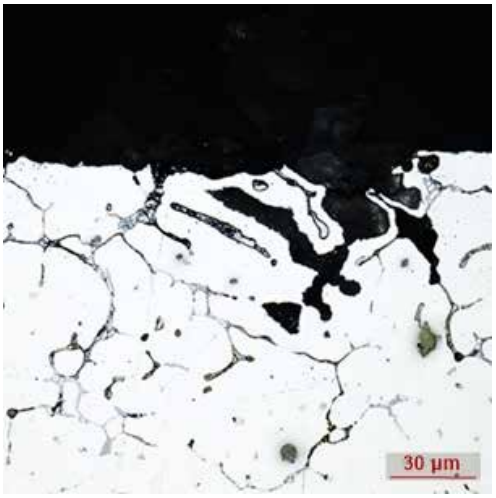

Figure 4: Microstructure of the sample after 480 h in a corrosive environment.

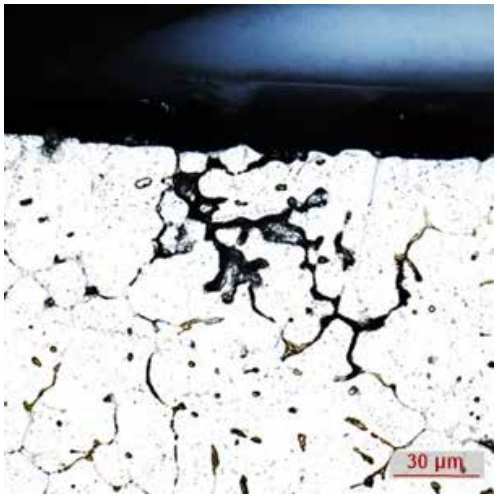

Figure 5: Microstructure of the sample after 720 h in a corrosive environment.

EDX ANALYSIS OF SAMPLE MORPHOLOGY

The study of the surface morphology of the samples was performed using electron microscopy. In all cases, a TESCAN VEGA 3 electron scanning microscope was used for imaging, while the samples were always studied at a magnification of 1,000x, 2,500x, and then 4,000x.

Figure 6 shows that in an area where IC occurs, corrosion products have penetrated into the α-matrix that surrounds them. An increased distribution of O was observed. This confirms the recording of the area EDX analysis and the quantification of the results of the area EDX analysis in both areas (**Figs. 6 and 7**), where the oxygen content was measured up to about 23% wt.

EVALUATION OF THE COURSE OF HARDNESS

Another evaluation of the experimental samples was to examine the course of hardness depending on the depth of occurrence of corrosion products, which are essentially intermetallic phases. The hardness of the sample without corrosion was 80 HV. The hardness decreases toward the core of the sample, as the amount of corrosion products decreases from the surface to the core of the sample.

CONCLUSION

Based on the performed experiments, five samples were made from EN AW 2024 alloy, which were subsequently subjected to a detailed examination, during which the influence of the corrosion environment on the structure of the material and its properties (hardness) was studied. Based on the performed analyses, the following conclusions were reached:

- After 168 to 240 hours of exposure to salt spray, an uneven distribution of pitting corrosion was found with a penetration of 16 mm below the surface of the material
- After 480 hours of exposure to salt spray, an uneven distribution of pitting and intergranular corrosion was found, which occurs in dendritic cores as these areas are depleted of Cu in the micro-segregation, and penetrates to a depth of 50 mm

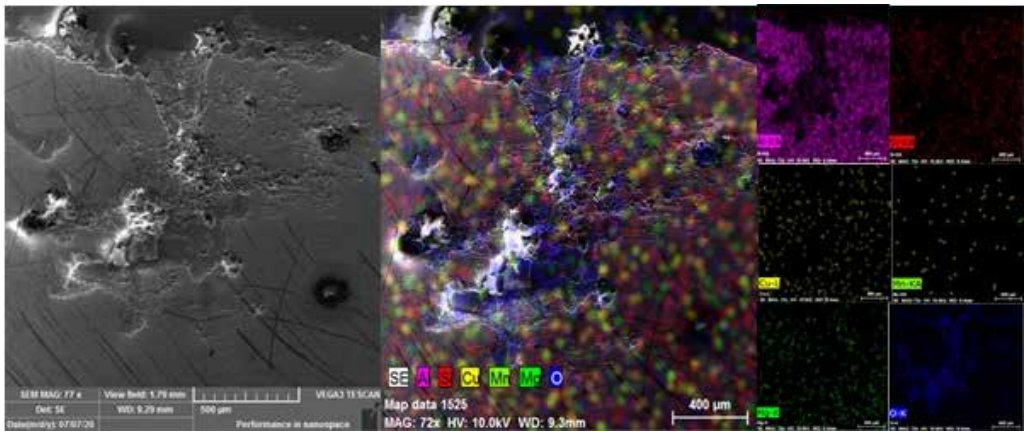

Figure 6: Microstructure of Sample C, elemental cross-sectional maps of the sample.

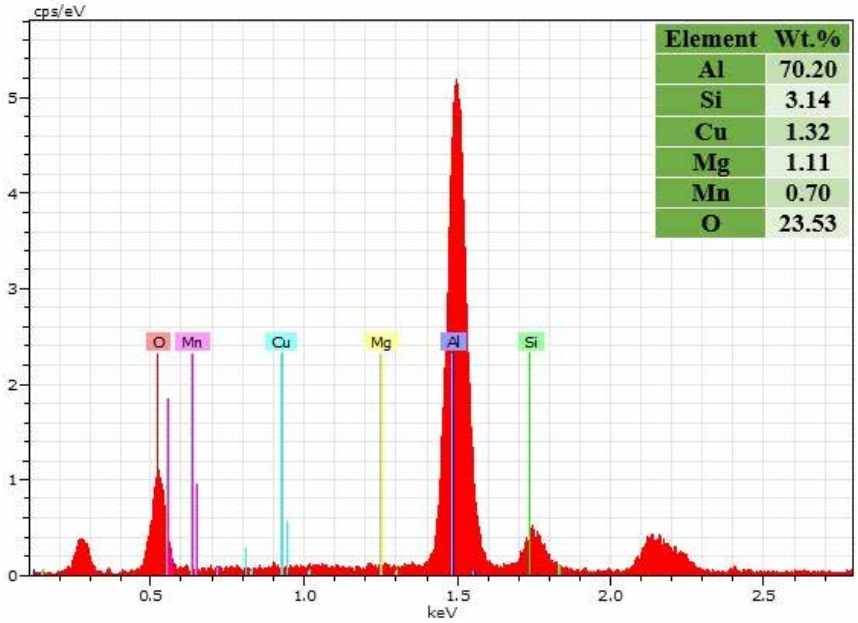

Figure 7: Area EDX analysis of a selected area from sample C and quantification of the results of area EDX analysis.

- For a sample after 720 hours of salt spray exposure, the microstructure shows an uneven distribution of pitting and intergranular corrosion closely associated with interdendritic phases, with penetration up to 95 μm below the alloy surface
- Samples after 480 and 720 hours show intergranular corrosion, which begins to act at grain boundaries that are rich in Al_2Cu and continues in areas of α-phase depleted by Cu; area EDX analysis confirmed areas of intergranular corrosion in the α-matrix, and an increased distribution of O was observed
- From the performed hardness analysis, it can be seen that the reduction of the hardness of the material is associated with the reduction of the number of Cu in the α-phase regions, which was consumed for the formation of corrosion products in the form of intergranular corrosion

REFERENCES

[1] *Lin, Y. C. et al. Effects of creep-aging processing on the corrosion resistance and mechanical properties of an Al–Cu–Mg alloy. Mater. Sci. Eng. A 605, 192–202 (2014).*

[2] *McNaughtan, D., Worsfold, M. & Robinson, M. J. Corrosion product force measurements in the study of exfoliation and stress corrosion cracking in high strength aluminium alloys. Corros. Sci. 45, 2377–2389 (2003).*

[3] *Eivani, A. R., Zhou, J. & Duszczyk, J. Mechanism of the formation of peripheral coarse grain structure in hot extrusion of Al-4.5Zn-1Mg. Philos. Mag. 96, 1188–1196 (2016).*

[4] *ČSN ISO 9227. Corrosion tests in artificial atmospheres - Salt spray tests. Eur. Stand. EN ISO 92272006 3, (2007).*

[5] *Kusmierczak, S. & Hren, I. Influence of Al-Si7Mg0.3 Alloy Modification on Corrosion Behaviour in the Salt Environment. Manuf. Technol. 19, 802–806 (2019).*

[6] *Zhou, C., Yang, X. & Luan, G. Effect of root flaws on the fatigue property of friction stir welds in 2024-T3 aluminum alloys. Mater. Sci. Eng. A 418, 155–160 (2006).*